$^{40}Ar/^{39}Ar$ thermochronology in the Ios basement terrane resolves the tectonic significance of the South Cyclades Shear Zone

MARNIE FORSTER*, OLEG KOUDASHEV, RUORAN NIE, SONIA YEUNG & GORDON LISTER

Structure Tectonics, Research School of Earth Sciences, Australian National University, Canberra 2601, Australia

M.F., 0000-0002-1240-4374; R.N., 0000-0002-7346-2674

**Correspondence: marnie.forster@anu.edu.au*

Abstract: We conducted ^{39}Ar diffusion experiments using potassium feldspar from the South Cyclades Shear Zone on Ios, in the Cyclades, Aegean Sea, Greece. Irradiated samples were step-heated in an ultra-high-vacuum resistance furnace attached to a mass spectrometer, thus also allowing $^{40}Ar/^{39}Ar$ geochronology. Conjoint inversion of these datasets allowed estimation of the relevant diffusion parameters, which were then used to forward model the effect of arbitrary temperature–time histories. Simulations used Monte Carlo methods to improve approximations to the observed age spectra. Two periods of rapid cooling could be inferred. The South Cyclades Shear Zone commenced operation during or shortly after the Eocene–Oligocene transition. Episodes of south-directed movement continued into Early Miocene time, however, with the footwall still hot enough to cause biotite ± garnet metamorphic mineral growth at the base of the overlying, already substantially exhumed, eclogite–blueschist unit. Since its footwall continued to cool, the South Cyclades Shear Zone was an extensional shear zone during both episodes of its operation.

Supplementary material: A description of our analytical methods, analysis data, $^{40}Ar/^{39}Ar$ procedure information and forward modelling data plus other relevant data are available at https://doi.org/10.6084/m9.figshare.c.4447973

How to make the distinction between a thrust- versus an extensional-detachment-related structure is one of the most difficult topics in structural geology. In this paper we show we can achieve this result if we can: (i) determine how temperature varied with time in the footwall, and/or in the hanging wall; and then (ii) link this thermal evolution to the development of fabrics and microstructures in the rocks affected by these movements. Such data can uniquely constrain the tectonic significance of an individual low-angle fault or shear zone and thus allow choice between these competing hypotheses (Fig. 1).

One might consider that this distinction should be made using sense-of-shear indicators, but these usually do not help. Regionally developed shear zones are typically warped and folded. Stretching can impose shear bands with opposing shear-sense around crustal-scale necking structures, and these later-stage shear bands confuse the recognition of shear-sense associated with the dominant fabric. In consequence, while sense-of-shear and variation in the trend of stretching lineations remain important and significant variables, they do not allow us to determine whether: (i) a specific ductile shear zone was associated with stretching of the crust overall, and linked to the operation of areally extensive detachment faults; or (ii) the shear zone in question represents the deeper structural levels of a megathrust, with brittle thrust faults in its more surficial expression.

Low-temperature geothermometers are also of limited value in dealing with this question. (U–Th)/He or fission track analyses using apatite and/or zircon record time only in temperature regimes wherein the rock has long ceased to be ductile. Similar limitations apply to high-temperature geochronometers such as U–Pb methods that date the formation of accessory minerals in magmas or in high-temperature metamorphic rocks. In contrast $^{40}Ar/^{39}Ar$ geochronology is of more direct interest, because the method provides timing data that coincide with the range of temperatures during which most exposed crustal rocks develop fabric. A key aspect of our research has thus been to integrate the theory and methods of $^{40}Ar/^{39}Ar$ geochronology to allow the interrogation of fabrics and microstructures to reveal the history of orogenesis in the ductile regime.

From: Bond, C. E. & Lebit, H. D. (eds) 2020. *Folding and Fracturing of Rocks: 50 Years of Research since the Seminal Text Book of J. G. Ramsay*. Geological Society, London, Special Publications, **487**, 291–313.
First published online May 23, 2019, https://doi.org/10.1144/SP487-2018-169

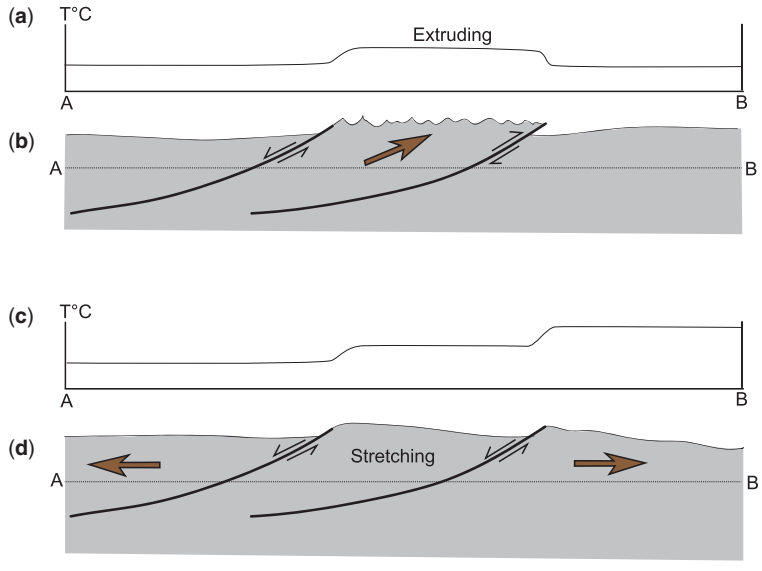

Fig. 1. Palaeotemperature at a specific depth will vary depending on the kinematics of major faults and shear zones: (**a, b**) across an extruding wedge; and (**c, d**) across a succession of detachment slices. The thermal history therefore allows choice between the thrust versus detachment hypothesis for an individual fault or ductile shear zone, thus providing an opportunity to resolve a long-standing debate as to the tectonic significance of the South Cyclades Shear Zone (SCSZ).

The Cycladic Archipelago

The Cyclades, Aegean Sea, Greece (Fig. 2) is a good place to demonstrate our progress, for several papers now assert a thrust interpretation for structures there that have previously been argued to be extensional (e.g. Huet *et al.* 2009; Xypolias *et al.* 2012; Aravadinou *et al.* 2016). Of particular interest are competing models for the origin of the South Cyclades Shear Zone (or SCSZ) on Ios (Fig. 3). One hypothesis (Huet *et al.* 2009) considers the SCSZ as a thrust, formed beneath the eclogite–blueschist belt while buoyancy drove its extrusion from a 'syn-orogenic' subduction channel. The alternative hypothesis is that the SCSZ is the ductile carapace of a metamorphic core complex formed on the northern margin of the closing Tethys, starting in earliest Oligocene time (Forster & Lister 2009). The core-complex model suggests that the eclogite–blueschist belt was significantly exhumed before it was thrust over the Ios basement terrane prior to SCSZ activity (Vandenberg & Lister 1996). Operation of the SCSZ was associated with partial exhumation of the Ios basement in the footwall of an earlier-formed terrane stack, followed by brittle extensional detachment faults that accomplished further exhumation.

The Cycladic archipelago provides spectacular exposures of a dismembered eclogite–blueschist belt overlying metamorphic core complexes. There is much to be learned as to: (i) the nature of Alpine orogenesis; (ii) how high-pressure rocks are exhumed; and (iii) the interaction of deformation with fluid and metamorphic processes. This, with the quality of outcrop, the ease of access and the convivial environment, makes the Cyclades a popular choice for student mapping camps and research projects. However, the resultant maps or cross-sections differ widely (e.g. for Sifnos, compare Avigad 1993; Groppo *et al.* 2009; Ring *et al.* 2011; Aravadinou *et al.* 2016; Roche *et al.* 2016). These marked differences in style or interpretation point to a number of problems in respect to the elucidation of the geological architecture – issues that need to be addressed if we are to progress our understanding of this outstanding natural laboratory for the study of structural geology and tectonics.

Xypolias *et al.* (2012) review some of differences in interpretation, and we add to their list. The least contentious propositions are that: (i) the eclogite–blueschist belt formed in association with a long-lived north- to NE-facing subduction zone (Jolivet *et al.* 2003; Jolivet & Brun 2010; Ring *et al.* 2010); (ii) south- to SE-directed rollback of the hinge of the subducting slab caused lithospheric extension and exhumation of metamorphic rocks (Lister *et al.* 1984; Jolivet & Faccenna 2000; Brun & Faccenna 2008; Husson *et al.* 2009); and (iii) the rocks involved were subject to continual

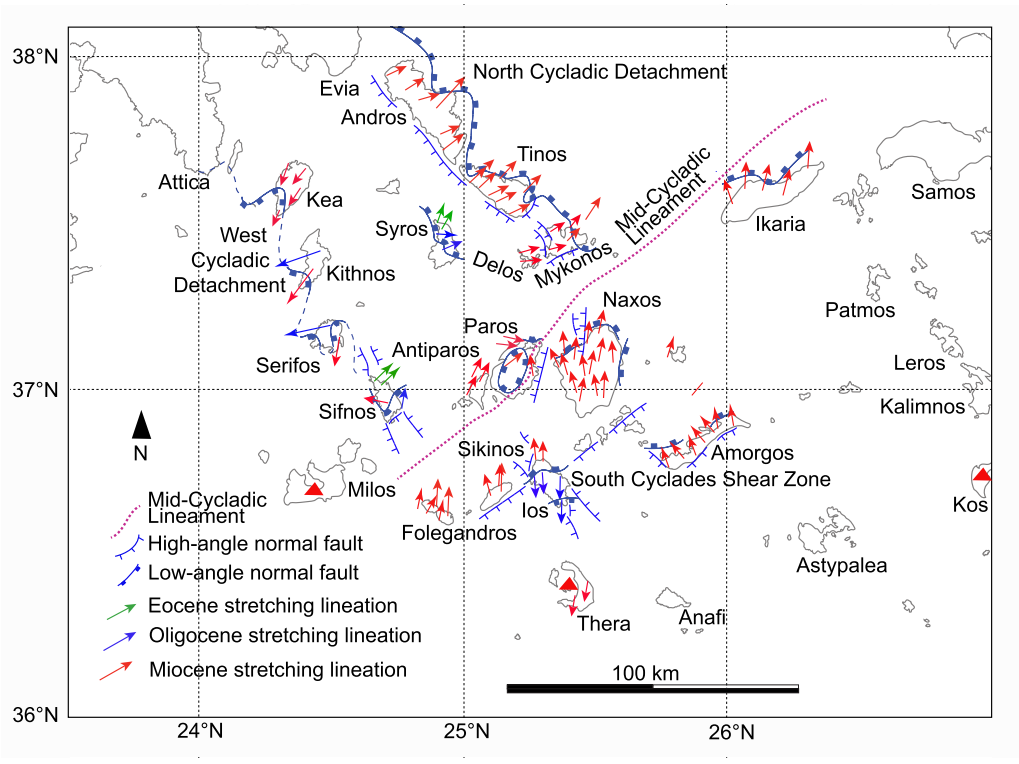

Fig. 2. Map showing the regional context of detachment structures and stretching lineations in the Cyclades, Aegean Sea, Greece. The position of the Mid-Cycladic Lineament (Walcott & White 1998) is modified to reflect its trace as mapped on Paros. Position of the West and North Cycladic detachment system shown schematically, modified from various authors. Variation in lineation trends is in excess of what can be shown at the scale illustrated, with trends as based on our own work and including the following authors: Augier *et al.* (2015), Forster & Lister (2009), Gautier *et al.* (1993), Grasemann *et al.* (2012), Jolivet *et al.* (2004*b*, 2010, 2013), Rosenbaum & Ring (2007), Schneider *et al.* (2011, 2018), Vandenberg & Lister (1996), Walcott & White (1998). Many shear zones that record Early Oligocene ages are also overprinted in Miocene time. Lineation trends change abruptly across the Mid-Cycladic Lineament, but this is due to overprinting in consequence of Miocene extension. The extrapolation of the South Cyclades Shear Zone is problematic because the throw on the several different sets of later high-angle normal fault systems is not constrained.

tectonism during the Alpine orogeny, whether this was 'continuous' (e.g. Cliff *et al.* 2017) or episodic as the result of a succession of accretion events (Lister & Forster 2009; Edwards & Grasemann 2009). There are also controversial questions such as: (i) whether the eclogite–blueschist belt exhumed as an entity (Jolivet *et al.* 2003) or as a succession of individual tectonic slices each with a distinct tectonothermal history (Forster & Lister 2005, 2009); or (ii) whether there were several generations of subhorizontal extensional shear zones and detachment faults. Other issues are described below.

When did high-angle normal faults form?

The topography of the Cyclades is dissected by intersecting arrays of high-angle normal faults (Mascle & Martin 1990), each array with distinct trends. Brun *et al.* (2016) suggests a change in tectonic style in the Pliocene, moving from distributed extension to the formation of high-angle normal faults defining tilt-block arrays. However, on Sifnos we have also mapped earlier formed tilt-block arrays that are truncated at their base by a low-angle detachment (see cross-section in Groppo *et al.* 2009). Hence the transition noted by Brun *et al.* (2016) might reflect the start of a new extension cycle, in the manner as described by Lister & Davis (1989) for the Cordilleran core complexes. In any case, the largely unspecified vertical throws on these high-angle faults make it difficult to correlate earlier-formed subhorizontal structures, confounding interpretations (in maps or cross-sections) that attempt to extrapolate individual low-angle structures from island to island (Fig. 2).

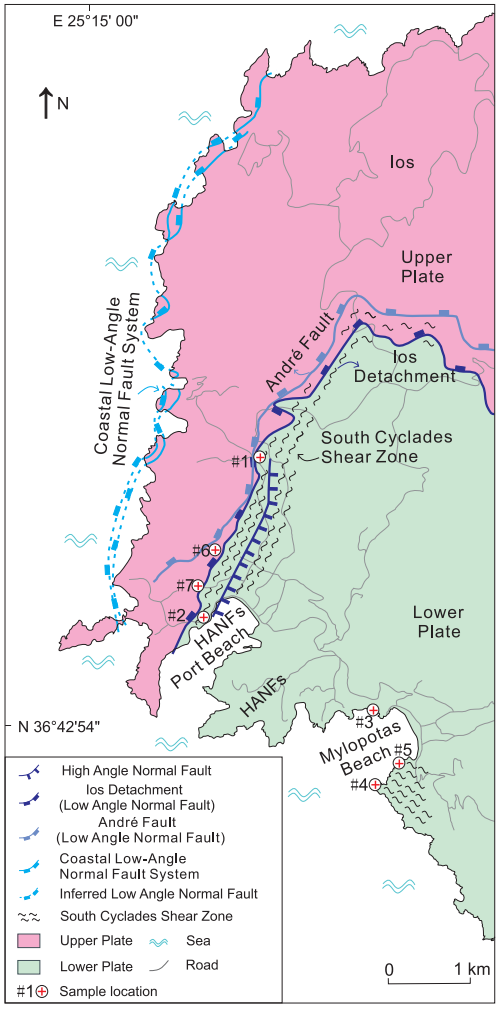

Fig. 3. Map of NW Ios with locations mentioned in the text. Detachment fault systems formed at three different ages are shown: (i) the Ios detachment; (ii) the André detachment, and (iii) the Western Coastal detachment system. Mylonites of the SCSZ are cut by listric normal faults related to the Ios detachment, and locally back-rotated into steeper orientations. The even later-formed Port Beach high-angle normal fault system also cuts the SCSZ and again back-rotates and steepens the SCSZ fabrics.

An episodic v. a continuous tectonic evolution?

There are differences in opinion as to the metamorphic evolution of these rocks, as set out by Huet *et al.* (2009, 2015). Issues that need to be resolved include whether: (i) the pressure–temperature–time (*P–T–t*) path followed by individual rocks was a relatively simple loop (e.g. Jolivet & Brun 2010), or convoluted, reflecting the effect of movements that produced the observed fabrics and microstructures (Forster & Lister 2005; Lister & Forster 2016); or whether (ii) the metamorphic evolution was a simple (M1–M2) retrogression to greenschist facies caused by percolation of fluids into eclogite–blueschist rocks (e.g. Schliestedt & Matthews 1987), or a well-defined sequence of metamorphic mineral growth episodes closely linked to the initiation and operation of crustal-scale extensional shear zones (e.g. Forster & Lister 2005; Lister & Forster 2009, 2016).

The exhumation of the high-pressure rocks was substantially complete before the onset of Oligo-Miocene extension (Avigad *et al.* 1997; Schmädicke & Will 2003; Chatzaras *et al.* 2006; Kokkalas *et al.* 2006). However, we argue that the Ios basement terrane was accreted in Late Eocene time when it underthrust the already substantially exhumed eclogite–blueschist belt. Eventually the basement terrane was sliced free from the subducting African slab and added to the terrane stack overlying the active subduction-zone megathrust. According to the tectonic mode switch model (Rawling & Lister 1999; Lister *et al.* 2001, figs. 6–9; Forster & Lister 2005, fig. 12; Forster & Lister 2009, fig. 11; Lister & Forster 2009, figs. 9 & 10), shortening occurs when buoyant (later-to-be-accreted) terranes arrive at a subduction interface. Stress buildup leads to thrusting, with each thrust slicing into the newly arrived terrane and excising individual tectonic slices. These slices are added in turn to the over-riding terrane stack (Lister & Forster 2009, fig. 11), thus defining its tectono-metamorphic stratigraphy. Subsequent horizontal stretching of the terrane stack is made possible because accretion frees the subducting slab from the hindrance of the (now-accreted) buoyant material that caused the tectonic mode switch in the first place. For this reason, we do not divide the history into a syntectonic- v. a post-tectonic phase. As noted by Edwards & Grasemann (2009), convergence and consequent tectonism continue, even today.

Tectonic sequence diagrams

We applied classic methodologies (e.g. Ramsay & Huber 1987), but we have also considered new developments in structural geology (e.g. Hobbs 2019) such as the method of tectonic sequence diagrams, or TSDs (Forster & Lister 2008). In Forster & Lister (2005) and Lister & Forster (2009, 2016) we document a succession of Eocene to Oligocene metamorphic episodes: (i) eclogite facies growth of omphacite and jadeite, Δ_{1B} at *c.* 53 Ma, with post-Δ_{1B} stretching; (ii) a succession of Δ_{1C} porphyroblastic growth events in the glaucophane + garnet blueschist facies, from *c.* 46–42 Ma, followed by exhumation in post-Δ_{1C} shear zones that are later recumbently folded; and (iii) transitional

epidote–albite blueschist facies (Evans 1990) with metamorphic mineral growth events, Δ_{1D} at *c.* 35–34 Ma, followed by exhumation in post-Δ_{1D} shear zones that are also later recumbently folded. This sequence of metamorphic mineral growth events (Fig. 4) is regionally consistent, with each growth episode linked to the subsequent formation of ductile shear zones and/or pure shear ductile stretching of the rock mass, e.g. Cliff *et al.* (2017). The use of TSDs is thus critical in allowing $^{40}Ar/^{39}Ar$ geochronology to be tied to the evolution of fabric and microstructure.

TSDs allow ready incorporation of the detail of event sequences discernable under the optical microscope, allowing the metamorphic evolution to be tied to the sequence of fabric-forming events and microstructural processes. When dates are linked to TSDs, microstructurally focused geochronology (e.g. Cliff *et al.* 2017) becomes a valuable tool for structural analysis. In this way we were able to demonstrate that the Cycladic metamorphic core complexes formed as the result of extreme stretching of the lithosphere during two separate events. The first of these stretching events occurred in Eocene–Oligocene time (Forster & Lister 2009) when the Ios core complex formed beneath a post-Δ_{1D} Early Oligocene shear zone. The core complex was later transected by Miocene north-sense ductile shear zones formed in association with the extreme extension that produced the North Cycladic core complexes, on Naxos and Paros (Urai *et al.* 1990; Buick 1991; Lee & Lister 1992; Gautier *et al.* 1993; Gautier & Brun 1994; Jolivet *et al.* 2013). Equivalent Early Oligocene extensional shear zones have now been recognized, e.g. on Serifos (Schneider *et al.* 2011), Syros (Lister & Forster 2016) and Sifnos. Huet *et al.* (2015) record ages on Andros that are consistent with the late stages of such Early Oligocene shear zones. These data imply a considerable lateral extent for such structures (Fig. 2), potentially connecting the SCSZ into an Oligocene equivalent of the Miocene West Cycladic detachment fault system (Grasemann *et al.* 2012).

The Ios metamorphic core complex

Ios (Fig. 3) was the first recognized of the Aegean metamorphic core complexes (Lister *et al.* 1984). Its discovery set the scene for the discovery of similar metamorphic core complexes scattered along the northern extants of Alpine Tethys (e.g. Jolivet *et al.* 1999; Verdel *et al.* 2007), including dozens of schists and gneiss domes in the northern reaches of the Himalaya, Karakorum and Tibet (e.g. Lee *et al.* 2004; Guo *et al.* 2008; Forster *et al.* 2011).

Tethyan core complexes

Significant differences distinguish Tethyan core complexes from their cousins in the North American Cordillera (G.H. Davis 1983; G.A. Davis *et al.* 1986; G.H. Davis *et al.* 1987; Lister & Davis 1989; Reynolds & Lister 1990). These differences can be summarized as: (i) a multiplicity of overprinting detachment faults and shear zones, including complicated interactions with high-angle normal faults; (ii) complex kinematics during the exhumation history; (iii) an absence of major breccia zones; and (iv) surficial deposits only in the very last stages of

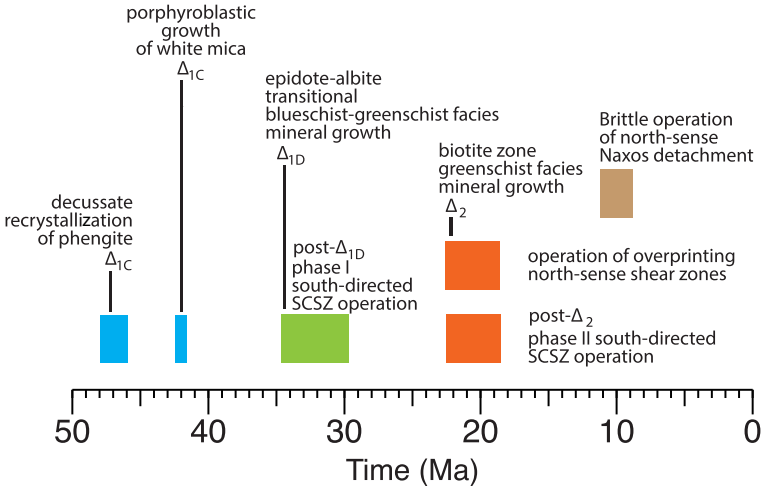

Fig. 4. Tectonic sequence diagrams showing a regionally consistent sequence of metamorphic mineral growth events, here illustrated for the base of the eclogite–blueschist sheets overlying the Ios basement terranes.

exhumation. These differences do not change one fundamental aspect of core complex formation and exhumation, however. These entities are typically caused by extension in the lithosphere over-riding a retreating subduction zone. In the case of the North American Cordillera, the Farallon Slab was collapsing into the mantle, with the zone of extending lithosphere far inland. In the case of the Aegean core complexes, the African slab was foundering. The essential difference was that Gondwanan basement terranes such as the Ios basement gneisses were progressively accreted to the Aegean terrane stack. The subduction zone megathrust became ever more distal in relation to the tectono-metamorphic evolution of individual slices in the terrane stack as time went on (Lister & Forster 2009).

In all metamorphic core complexes, detachment faults are brittle structures that transect earlier-formed shear zones. The ductile shear zones appear to accommodate the bulk of the movement, although the approximate spatial coincidence of later-formed detachment faults with earlier-formed ductile shear zones implies that the detachment faults feed into equivalent ductile shear zones at depth (Lister & Davis 1989). In consequence, the evolution of these extensional systems must be viewed as both progressive and episodic (cf. Brun *et al.* 2016). Ios is a typical Tethyan core complex in that complex kinematics were experienced during its long exhumation history (Vandenberg & Lister 1996; Forster & Lister 1999*a*, *b*; Huet *et al.* 2009). The south-sense shear zones were transected by north-sense shear zones, and by a multiplicity of low-angle brittle detachment faults that dissect the system and overprint earlier formed structures (Forster & Lister 1999*a*, 2009), e.g. the late-formed André Fault that transects the south-directed listric normal faults (Figs 5c & 6) that juxtapose the Cycladic eclogite–blueschist belt against the metamorphic basement.

South-dipping high-angle normal faults also dissect Ios, and other islands in the Cycladic archipelago, but these have rarely been included in published cross-sections. High-angle normal faults explain the locally steep SCSZ fabrics in the northernmost exposures of the Ios basement, since back-rotation (Fig. 6) leads to steepening of north-dipping fabrics. In contrast, because fabrics in the south of the Ios dome originally dipped more steeply to the south, back-rotation led fabrics in the south to become more gently inclined. Earlier-formed south-vergent listric normal faults also led to the local steepening of fabrics in the north, with fabrics near the Ios Detachment rotated past the vertical (Fig. 5c).

The South Cyclades Shear Zone

The carapace of the Ios schist and gneiss dome is defined by the SCSZ. The SCSZ was later cut by brittle detachment faults formed with the same south-directed sense of movement (Fig. 5a–c, locations 1 and 2). The core complex was also dissected by later, Oligo-Miocene, north-directed extensional ductile shear zones and associated brittle detachment faults, e.g. the north-directed André Fault, mapped by Forster & Lister (1999*a*), and a major north-directed greenschist facies shear zone in the very north of the island.

Huet *et al.* (2009) argued that the SCSZ cumulated strain during a long period of south-directed thrusting associated with extrusion of the Cycladic eclogite–blueschist belt, after its initial subduction. However, earlier-formed fabrics and microstructures in the eclogite–blueschist belt formed before SCSZ operation, as attested to by intervening periods of folding. Our mapping shows earlier-formed glaucophane lineations re-oriented in post-Δ_{1D} shear zones.

Forster & Lister (2009) show that the SCSZ formed during the Eocene–Oligocene stretching event, subsequent to earlier episodes of high-pressure metamorphism. It was re-activated with the same south-sense in the Oligo-Miocene stretching event and overprinted by north-sense shear zones. The fabrics in the SCSZ immediately below the Ios detachment are the most intense where the top of the SCSZ is exposed on scarps of the Port Beach high-angle normal fault system (Fig. 5b). The outcrop of the SCSZ on these scarps displays south-sense shear bands, including in the immediate vicinity of the Ios detachment. On the western flank of the Ios dome (e.g. locations 3, 4 and 5), coarse augengneiss also crops out, with the south-directed shear sense spectacularly recorded by large K-feldspar porphyroclasts (Fig. 5d). Intense north-directed shear zones (Fig. 5e) dissect the schist–gneiss contact, and these destroy the large K-feldspar porphyroclasts.

Two samples (both collected in 2001) were chosen at location 5, both described in Forster & Lister (2009). In this paper we invert these data to obtain an estimate of the variation of temperature with time during the geological history to which each sample was subjected. Sample AG01-02 (or AG02-01 in Forster & Lister 2009) is from a deformed Hercynian granitoid in the Ios basement, about 100 m below the projected location of the Ios Detachment (location 5 on Fig. 3), within the SCSZ. It is dominated by south-sense shear bands. The results of its analysis are shown in Figures 7–9, with details in the Supplementary Information. The second sample (AG01-01) is from a narrow (centimetre-scale) north-sense shear zone that overprints the SCSZ in a location immediately adjacent to AG01-02 (Forster & Lister 2009). The results of its analysis are shown in Figures 10–13, again with details given in the Supplementary Information. K-feldspar has grown in pressure shadows around

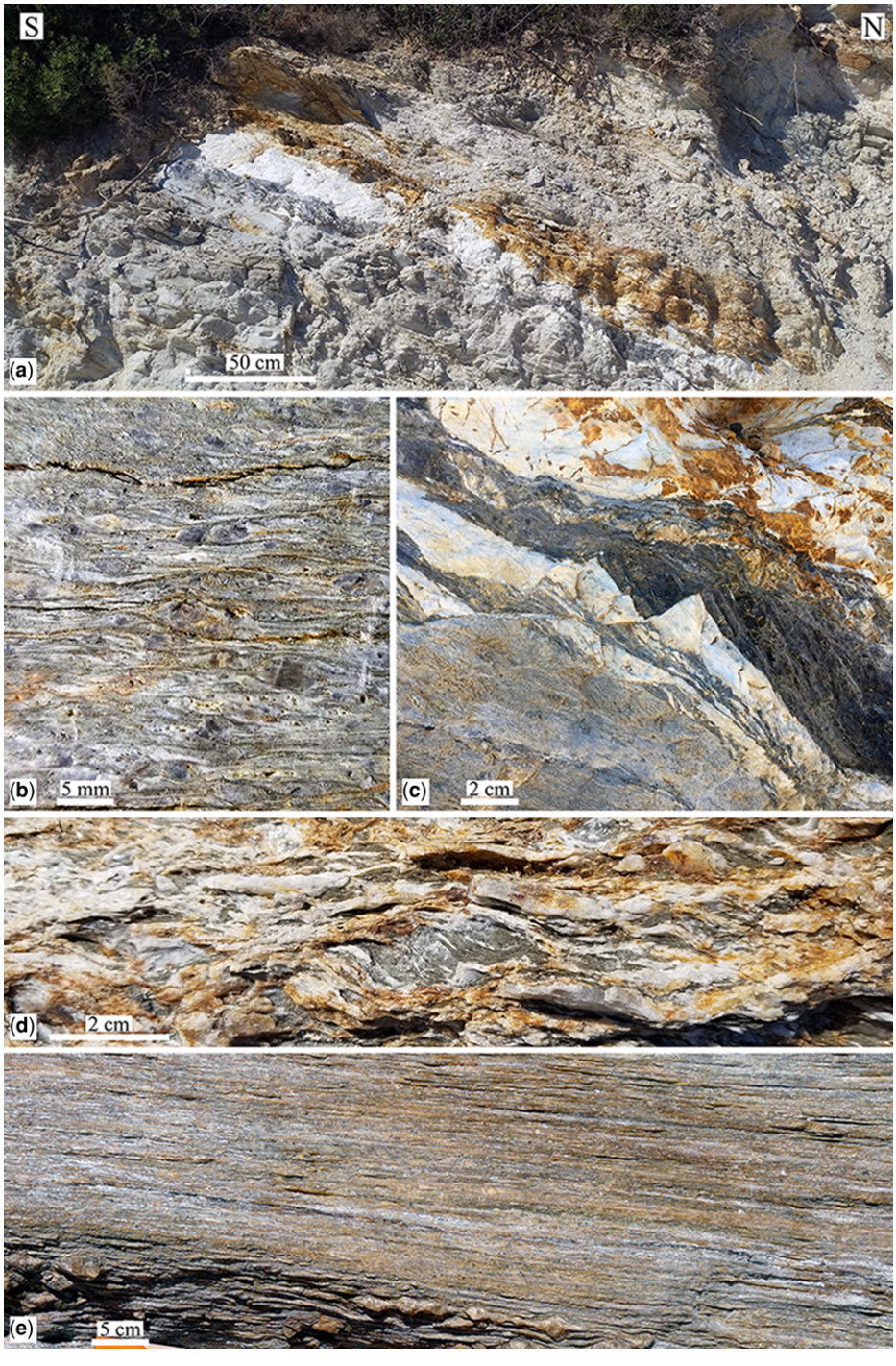

Fig. 5. The Ios Detachment Fault well exposed in a roadcut (**a**) in the scarp of the Port Beach high-angle normal fault system (at location 1 in Fig. 3). In (**b**) intense south-sense mylonites in the SCSZ, with remnant K-feldspar porphyroclasts (at location 2). South-directed listric normal faults (**c**) at location 1 incise into the SCSZ, and cause steepening of the fabric. Coarse augengneiss (**d**) at location 3 with south-sense shear bands. Intense strain in a north-directed overprinting shear zone (**e**) at location 4.

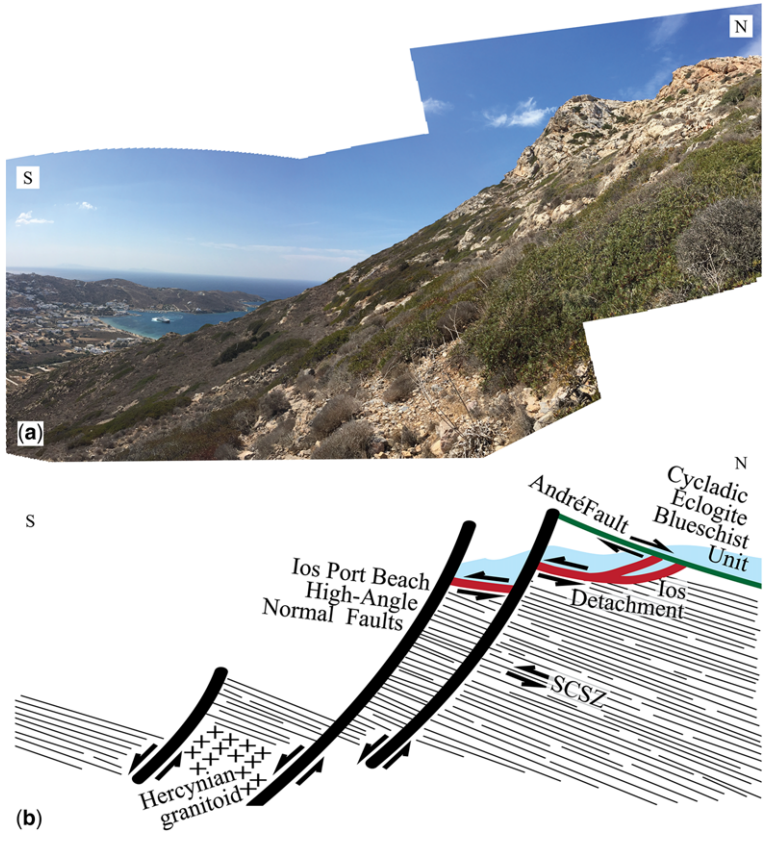

Fig. 6. The scarp of the Port Beach high-angle normal fault system (**a**) with the outcrop of the south-directed Ios detachment (**b**) and the overprinting north-directed André Fault.

older porphyroclasts which are progressively destroyed (Fig. 5d). The north-sense shear zones destroy the relict K-feldspar porphyroclasts (Fig. 5e), so AG01-01 yields a similar lower limit of 16.4 ± 0.1 Ma, but the relict *c.* 33.5 Ma population has disappeared. This limits the thermal history information that can be obtained from this sample. Since the *c.* 33.5 Ma steps in AG01-02 (Fig. 7) were not present in the north-sense shear zone sampled in AG01-01 (Fig. 10), Forster & Lister (2009) concluded that the SCSZ had commenced operation some time in the period 35–34 Ma.

Quantitative $^{40}Ar/^{39}Ar$ thermochronology

Here we report results using a newly developed technique called conjoint inversion to extract information from the Arrhenius plot, the comparative radius plot and the measured age spectrum, using these two samples from the SCSZ. Quantitative thermochronology requires specification of the diffusion parameters, thus enabling numerical models that can simulate the effect of temperature with time.

UHV diffusion experiments using ^{39}Ar

Based on the assumption of an initial geometry, data from ultra-high-vacuum (UHV) diffusion experiments using ^{39}Ar can be converted into D/r^2 measurements, where D is diffusivity and r the radius of the diffusion domain. Plotted against the inverse of absolute temperature, the resulting Arrhenius data (Figs 7 & 10) can be inverted to obtain estimates of the diffusion parameters, enabling further inversion to produce temperature histories capable of simulating the observed age spectra. UHV diffusion experiments require temperature to be calibrated accurately, using the melting point of several different metals. Each step-heating experiment produces one $^{40}Ar/^{39}Ar$ age measurement, corrected for interference from Ca and Cl contaminants, and in retrospect (after back-calculation) the percentage release of the ^{39}Ar isotope. The ramping up and ramping

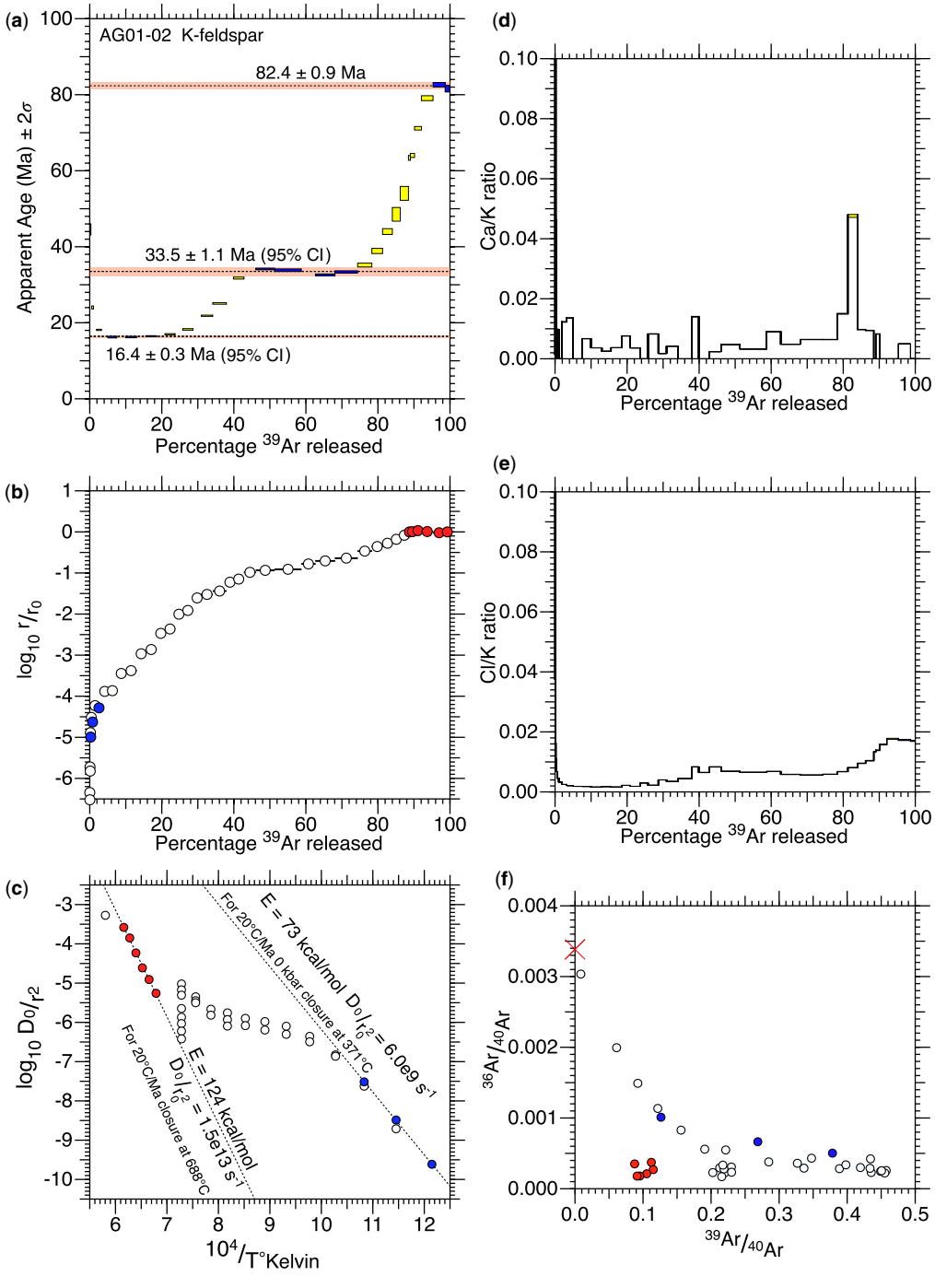

Fig. 7. $^{40}Ar/^{39}Ar$ geochronology for a furnace-step-heating experiment using sample AG01-02 from the SCSZ (location 5). The age spectrum (**a**) excludes cleaning steps. In (**b**) the comparative radius plot is based on the highest activation energy estimated using the fundamental asymmetry principle in the Arrhenius plot (**c**). Ratios of Ca/K (**d**) and Cl/K (**e**) estimated from ^{37}Ar and ^{38}Ar respectively. York plot (**f**) showing data quality. The steps with significant air contamination contribute less than 0.5% of the total volume.

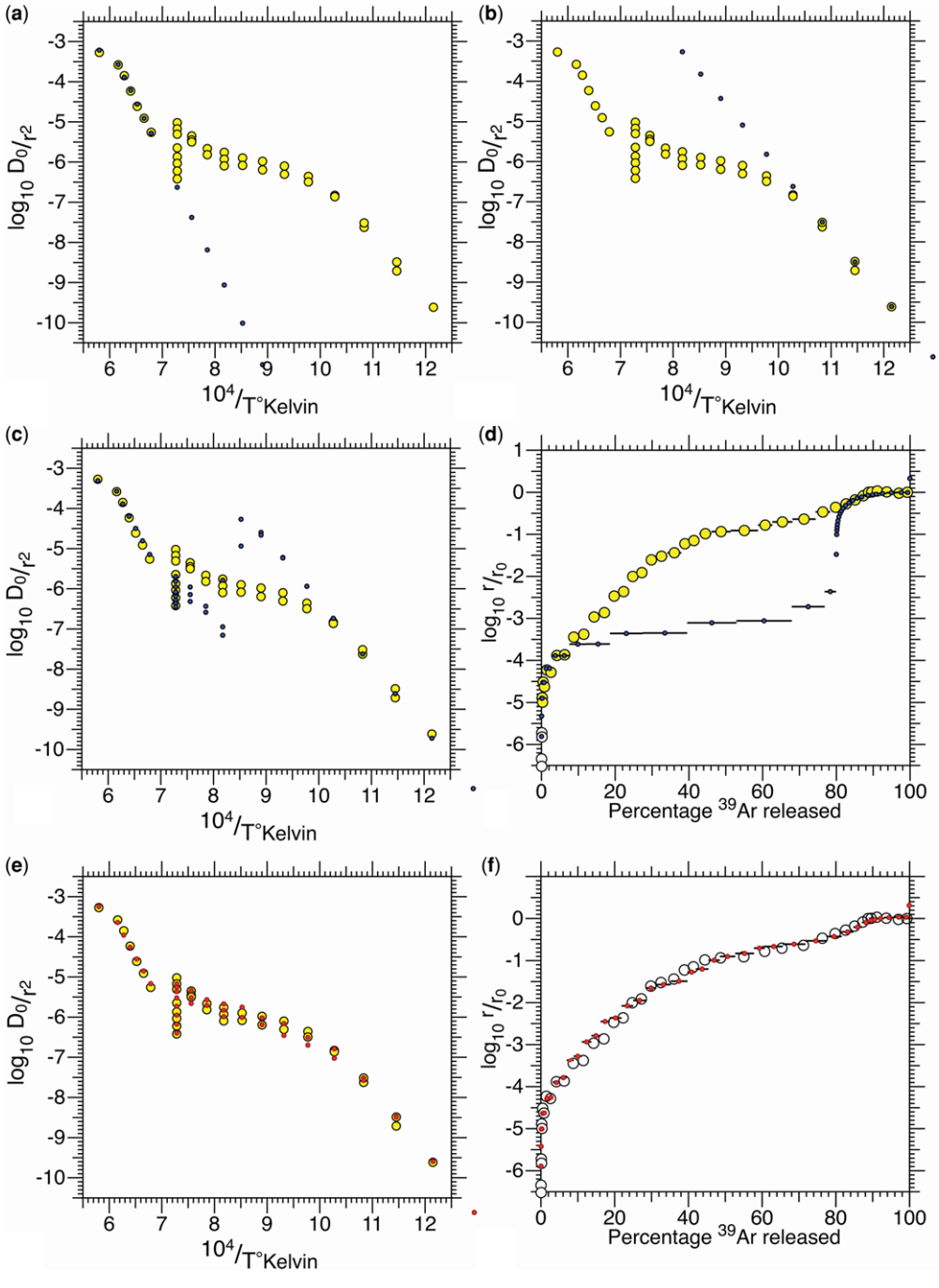

Fig. 8. The diffusion parameters for the most (**a**) and least (**b**) retentive diffusion domains can be estimated in isolation using the Arrhenius plot, by application of the fundamental asymmetry principle. In (**c**) these estimates are used to forward model the release of ^{39}Ar, to compare observations with model predictions. The effect of individual diffusion domains must be summed. The comparative radius plot (**d**) suggests that the volume of the retentive domains must be between 10 and 20% of the total volume. The fit can be improved considerably by assuming a fractal geometry, with several iterations of size and radius. This fit is obtained using Monte Carlo methods and conjoint inversion by simultaneously improving the fit on both the Arrhenius plot (**e**) and the comparative radius plot (**f**).

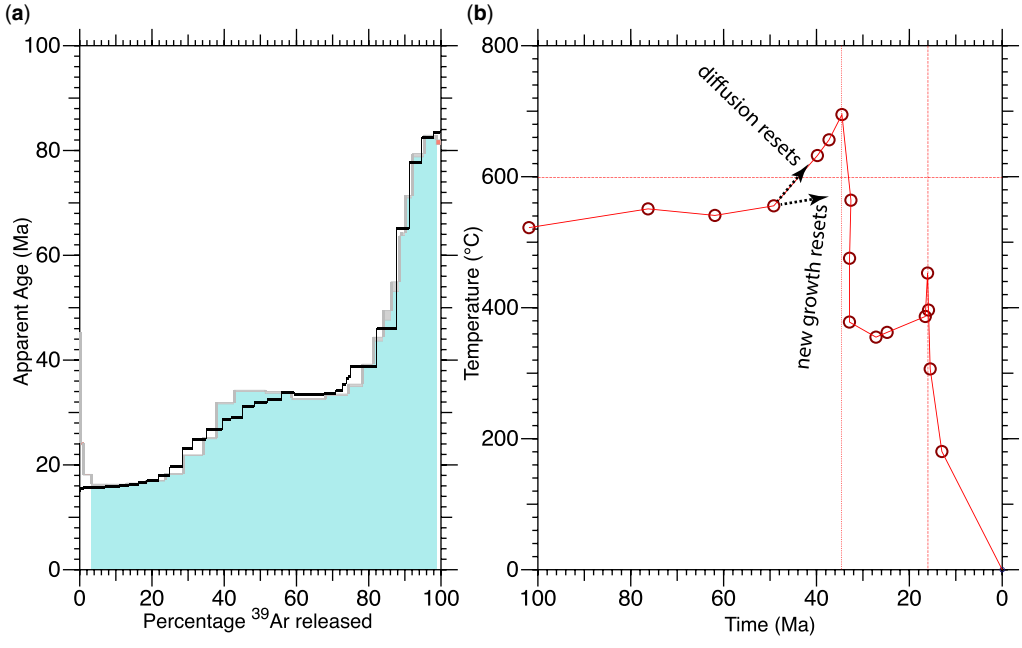

Fig. 9. Forward modelling using the diffusion parameters estimated from the UHV diffusion experiment with sample AG01-02. Using these data (provided in the Supplementary Information), the *MacArgon* program allows simulation of the age spectrum (**a**) that results from the temperature history (**b**). Monte Carlo methods were applied to minimize the least squares approximation to the selected steps (shaded in light blue) in the measured age spectrum. New growth of K-feldspar at *c.* 34 Ma would allow temperature to remain at <*c.* 550°C. The temperature rises in the simulation because resetting at this time was by solid-state diffusion alone.

down of temperature during each measurement need also to be abrupt, so that the equations used to calculate percentage loss produce reasonable approximations. Step-heating schedules need to be designed to uniformly populate the Arrhenius plot, as discussed in Lister & Forster (2016).

Conjoint inversion of Arrhenius data and age spectra

It is difficult to estimate the diffusion parameters from a complex Arrhenius plot. We suggest that there are 'core domains' that are highly retentive, with 'rim domains' that are far less retentive. The fundamental asymmetry principle (Forster & Lister 2010) allows estimation of their diffusion properties (Figs 7c & 10c), but this method requires the volume ratio to be independently estimated using the r/r_0 plot (Fig. 8). This is not an accurate method, however, as gas release from an individual domain does not occur in isolation. Therefore the *eArgon* program was modified to include the *Wunderkind* inversion routines. These use a *Monte Carlo* process seeded from estimates of the diffusion parameters. Individual threads computationally climb from a specific seed towards a best fit, determined conjointly by comparison with the Arrhenius plot and the r/r_0 plot. The methods of conjoint inversion require a decision tree, in this case: (i) weighting to avoid breach of the Fundamental Asymmetry Principle; and (ii) perturbation of the diffusion parameters to improve the least-squares fit on either or both the Arrhenius plot and the r/r_0 plot, with no reversion allowed.

The method can be described by analogy. The *Wunderkind* inversion routines drop individual 'climbers' (or seeds) at different locations in a mountainous landscape, with no prior knowledge of its topographic variation. Each climber begins to climb, and after a while, we compare how high different individuals have gone in order to decide which seeds have produced the most favourable outcome in terms of the goodness of fit. The routines vary activation energy, normalized frequency factor and relative volume, as well as the geometry parameters needed to describe a fractal. The most difficult variable is the number of fractal iterations allowed in order to describe the 3D 'roughness' of an individual diffusion domain. Because this number is discrete, we need to include judgements as to the morphology of an age spectrum that a particular fractal is

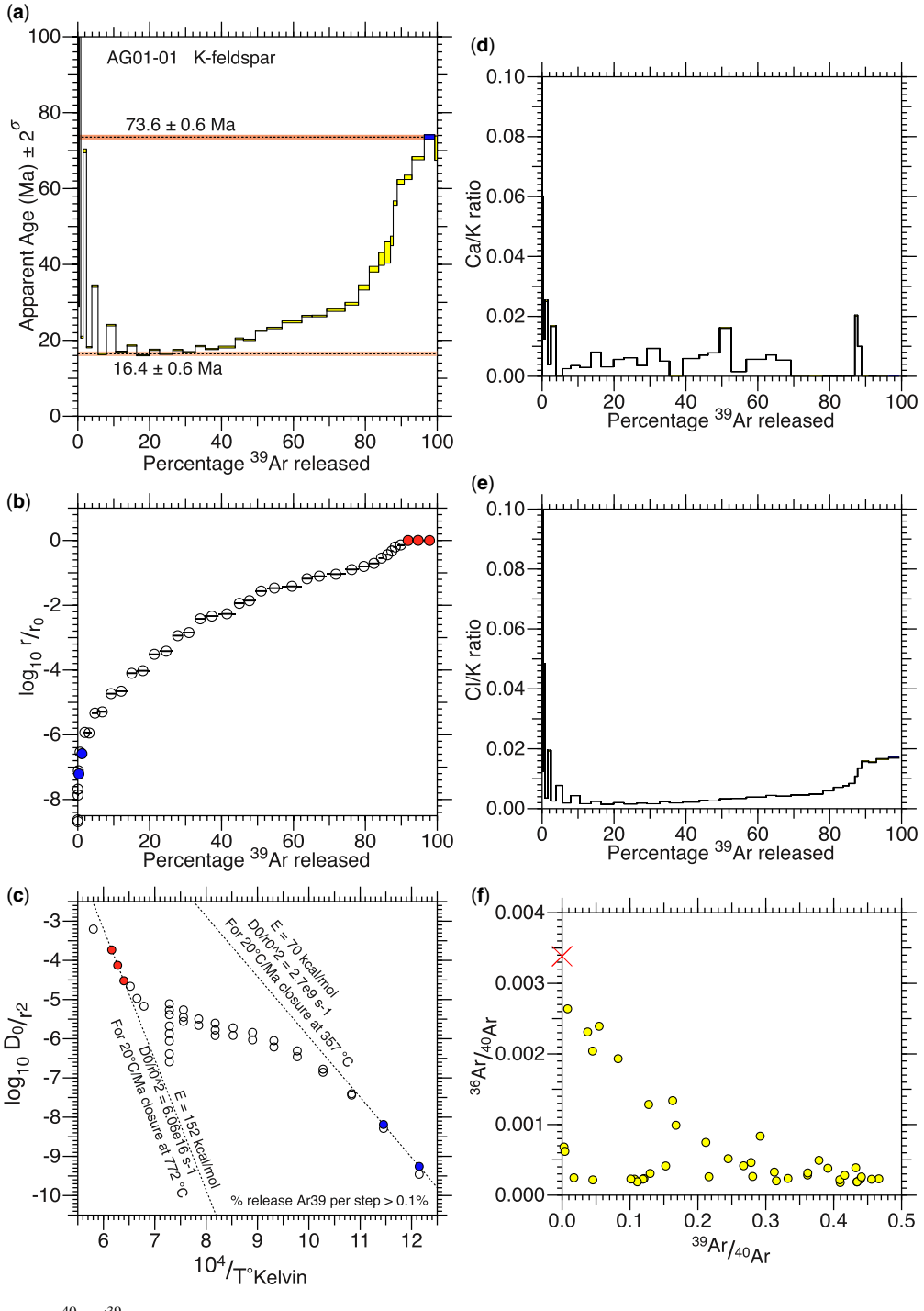

Fig. 10. $^{40}Ar/^{39}Ar$ geochronology for a furnace-step-heating experiment using sample AG01-01 from the SCSZ (location 5). The age spectrum (**a**) excludes cleaning steps. In (**b**) the comparative radius plot is based on the highest activation energy estimated using the fundamental asymmetry principle in the Arrhenius plot (**c**). Ratios of Ca/K (**d**) and Cl/K (**e**) estimated from ^{37}Ar and ^{38}Ar respectively. York plot (**f**) showing data quality. The steps with significant air contamination contribute less than 0.5% of the total volume.

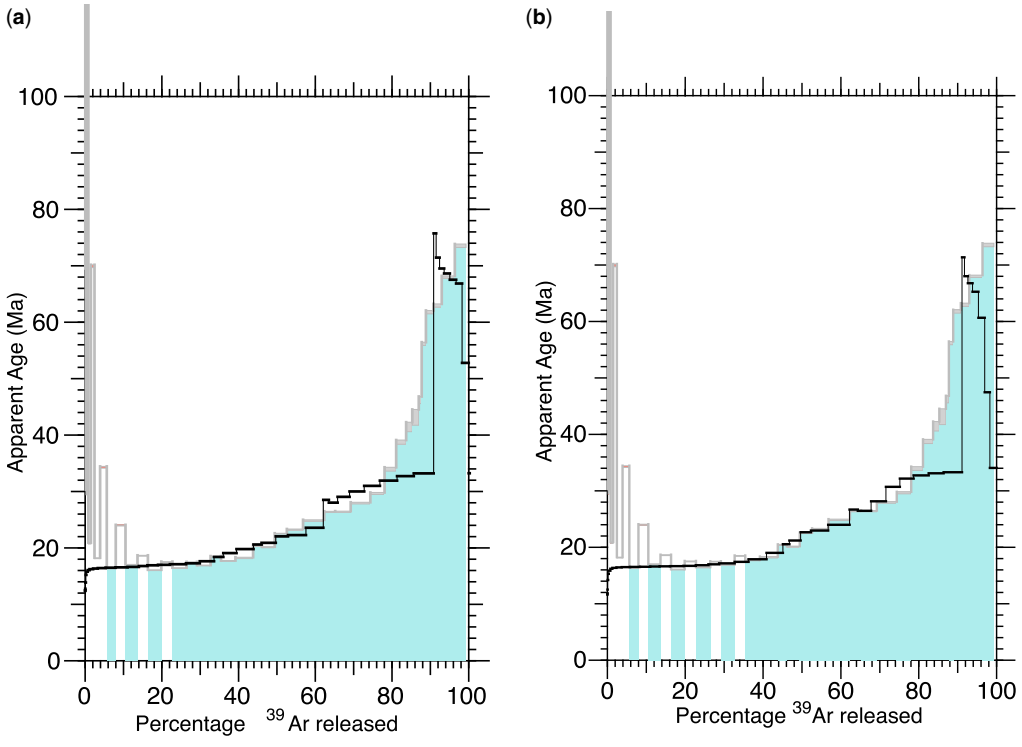

Fig. 11. Conjoint inversion also allows inclusion of considerations as to the morphology of the fit with the measured age spectrum. A poor fit is obtained with a few iterations of the fractal approximation to diffusion domain geometry: in particular all simulations show an age step as shown (**a**). Increasing the number of fractal iterations removes this effect, allowing an improved fit with the morphology of the measured age spectrum. In (**b**) the abrupt increase in age at 62% gas release in the simulated spectrum has disappeared, allowing a better fit to the morphology of the measured age spectrum.

capable of reproducing. When the number of fractal iterations is low (e.g. Fig. 11a), the spectrum jumps between sequences of smoothly progressing age steps. Increasing the number of fractal iterations continues to allow a good fit to the Arrhenius data and to the r/r_0 plots (Fig. 12), but now with a smoother variation of age steps (Fig. 13). Hence, the choice of fractal parameters must be refined, by iteration, with the morphology of the simulated spectrum used as an independent parameter.

Using the diffusion parameters thereby inferred, the *MacArgon* program then allows forward modelling of the effect of different temperature histories. Selected steps in the reference spectrum are used as control points, with *Monte Carlo* methods minimizing the sum of least square deviations between measured and simulated spectra. The results (Figs 9 & 13) show two periods of rapid cooling, one around *c.* 34 Ma and the other commencing around *c.* 18 Ma. Sample AG01-01 has suffered considerable microstructural modification after the *c.* 34 Ma event, so its memory of that event is lacking. Similarly, sample AG01-02 suffered significant microstructural modification during the *c.* 34 Ma event, and these effects also need be taken into account. The thermal excursion above 550°C (Fig. 9) may be an artefact, for example. New growth of retentive K-feldspar at *c.* 35 Ma would allow a temperature history without the need for a thermal spike to reset the 'argon clock' in these domains at that time.

Discussion

Argon enters the retentive zone

During the time that the SCSZ has been studied, a progression has taken place in our understanding of mineral retentivity in respect to argon diffusion. This began when Baldwin & Lister (1998) focused on the tectonic significance of a thermal event on Ios they assumed to have taken place at *c.* 14 Ma. They recognized that the remarkable heterogeneity in the distribution of $^{40}Ar/^{39}Ar$ age in the Ios

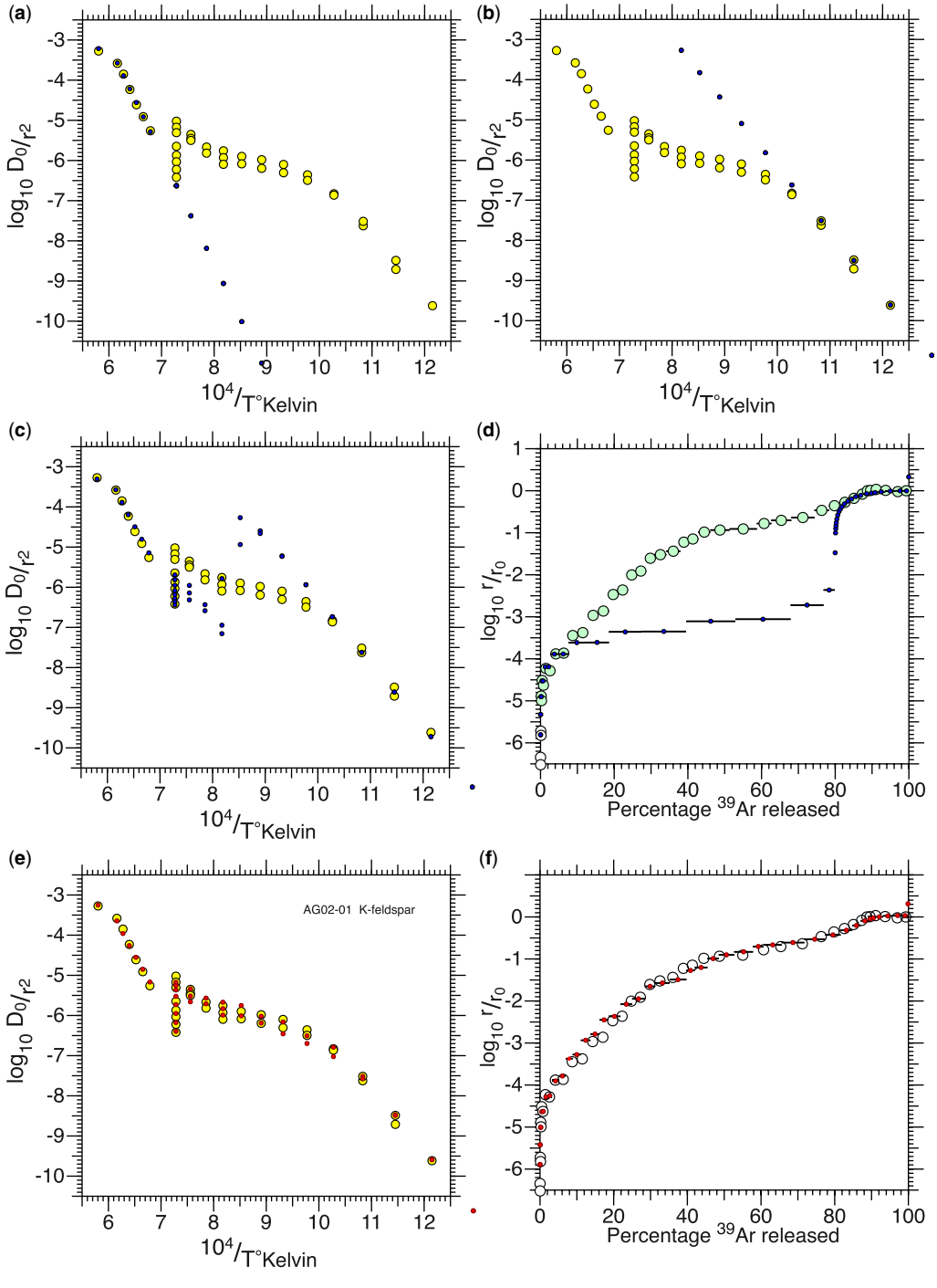

Fig. 12. The simulated Arrhenius data (**a**) and the corresponding comparative radius plot (**b**) for sample AG01-01, assuming a few fractal iterations. Increasing the number of fractal iterations allows an improved fit with the measured Arrhenius data (**c**) and the corresponding comparative radius plot (**d**). In (**e**) and (**f**) the fit is shown after Monte Carlo inversion has sought the best fit, with variation allowed in all parameters, including in the number of fractal iterations and the size and radius parameters.

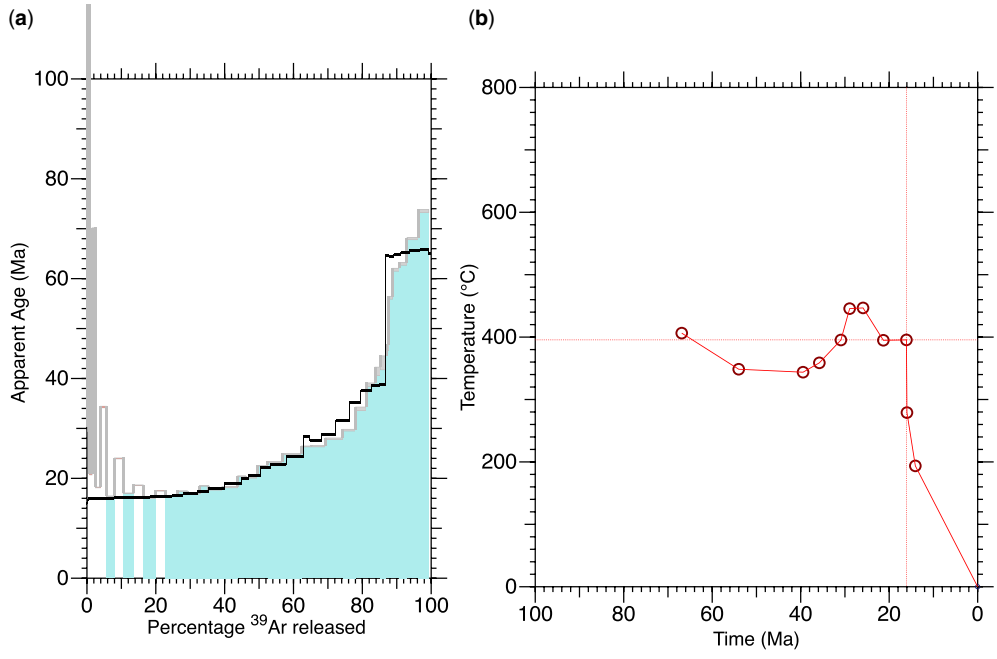

Fig. 13. Forward modelling using the diffusion parameters estimated from the UHV diffusion experiment with sample AG01-01. Using these data (provided in the Supplementary Information), the *MacArgon* program allows simulation of the age spectrum (**a**) that results from the temperature history (**b**). Monte Carlo methods were applied to minimize the least squares approximation to selected steps (shown in blue) from the measured age spectrum. Most porphyroclasts present prior to the operation of the north-sense shear zones have been destroyed. Owing to this microstructural modification the earliest steps of this temperature history must be considered problematic.

basement implied that these were not 'cooling ages' so the concept of 'closure temperature' had limited relevance to these rocks. Deformation and metamorphism had taken place in the Argon Partial Retention Zone. This work set the stage for the gradual recognition that $^{40}Ar/^{39}Ar$ age variation correlated with the relative age of the different microstructures (Forster & Lister 2005), a factor made even more evident by the application of the method of asymptotes and limits to the interpretation of $^{40}Ar/^{39}Ar$ age spectra (Forster & Lister 2004).

Building on the methods of analysis pioneered by Lovera *et al.* (1997, 2002), the *eArgon* computer code was then written to approximate the effect of fractal geometries on diffusion domains, and to allow the inversion of Arrhenius data. Thereby it was ascertained that minerals such as potassium feldspar (Forster & Lister 2010; Forster *et al.* 2015) or phengitic white mica (Forster & Lister 2013) may be far more retentive of argon than was considered to be the case. This means considerably higher closure temperatures, and that $^{40}Ar/^{39}Ar$ geochronology in consequence could be able to far better span the temperature regime relevant to structural geology. In many circumstances $^{40}Ar/^{39}Ar$ geochronology could be used for direct dating of the timing of microstructural events. This means that it would be less useful as a low-temperature thermochronometer, however.

Baldwin & Lister (1998) reported $^{40}Ar/^{39}Ar$ geochronology that provided the first hint that the SCSZ fabrics were remnant from an Eocene–Oligocene shear zone that had operated until at least *c.* 31–32 Ma. Similarly, the modelling results in this paper support the conclusion, based on microstructure, that the SCSZ had commenced its operation by *c.* 34 Ma (Forster & Lister 2009), and that its operation continued until *c.* 16 Ma. The overprinting of blueschist assemblages at the base of the upper plate by biotite ± garnet (Fig. 14) Δ_2 Barrovian assemblages formed during south-directed ductile shear further supports the suggestion that south-sense SCSZ operation continued in the Miocene (Fig. 4).

The thermal response to detachment faulting

Figure 15 shows the evolution of temperature above and below an extensional detachment, based on formulae in Voorhoeve & Houseman (1988). The first calculations (Fig. 15a, b) assume instantaneous displacement on a detachment fault: (i) with relative displacement of 30 km on a fault dipping at 22.5° in a

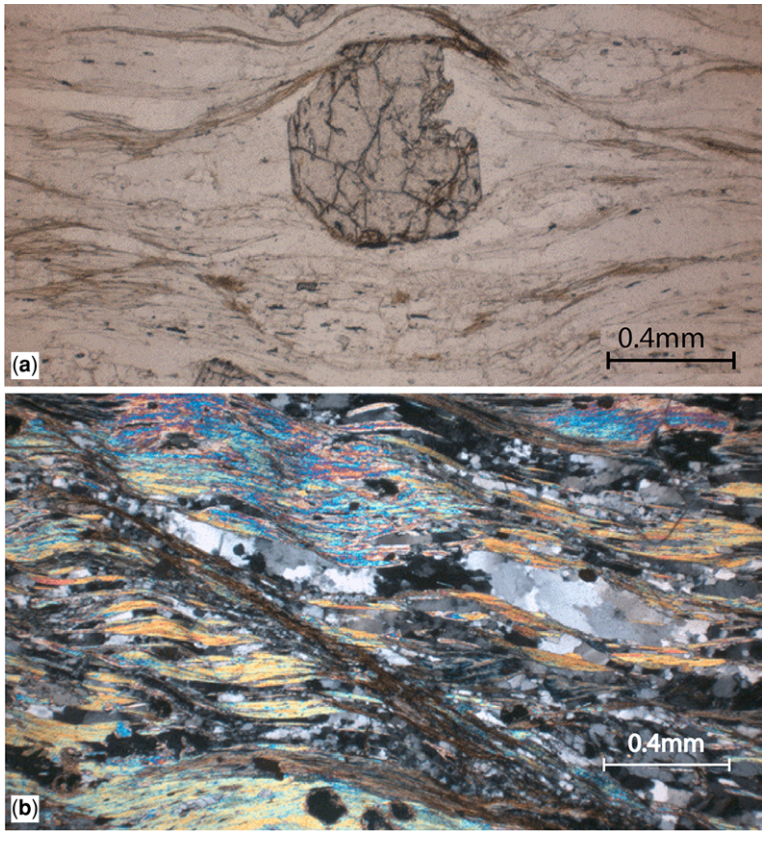

Fig. 14. Biotite locally occurs in shear bands in the eclogite–blueschist slices, immediately above the Ios detachment: (**a**) in shear bands near earlier-grown garnet porphyroblasts (plane-polarized light; AG10-46, location 6); and (**b**) in shear bands through schist with overprinting younger euhedral garnet (AG08-46, location 7). This demonstrates that the base of the upper plate became relatively hot, reaching biotite + garnet greenschist Barrovian facies conditions, driven by its juxtaposition against the exhuming Ios basement.

25°C/km geotherm; and (ii) 16 km on a fault dipping at 30° in a 30°C geotherm. These diagrams show the rapidity with which thermal relaxation results in heating of the upper plate, and in cooling of the lower plate. Rocks close to the detachment (or in the ductile shear zone) almost immediately adjust to the temperature averaged between upper plate and lower plate during movement. The speed of conductive thermal relaxation is such that adjustments to the geotherm are substantially complete within 0.1 Ma, at least for rocks within 2 km of the interface.

The remaining diagrams show the temperature history: (i) 100 m below the detachment (Fig. 15c, d); and (ii) 100 m above the detachment (Fig. 15e, f). The geometry of detachment ensures that the upper plate heats pervasively above a detachment system, even though cooling of the lower plate takes place at the same time. The interface adjusts rapidly to the average temperature, so that measurements within 100 m of the contact are not reliable estimators of the magnitude of relative displacement across an individual detachment system (cf Reiners & Brandon 2006). After movement ceases, the upper plate cools only slowly, because the length scale then includes the lower plate. Rapid cooling ensues only when the upper plate finds itself in the lower plate of a later-formed detachment system.

Thomson *et al.* (2009) inferred timing of the Ios detachment based on lack of age variation from the upper plate to the lower plate. The modelling (above) shows this to be a misconception.

Microstructures at the base of the upper plate

Microstructures also potentially allow determination of the tectonic significance of a major ductile shear zone. Rocks above a major thrust will be hotter than those below, but they will cool rapidly during

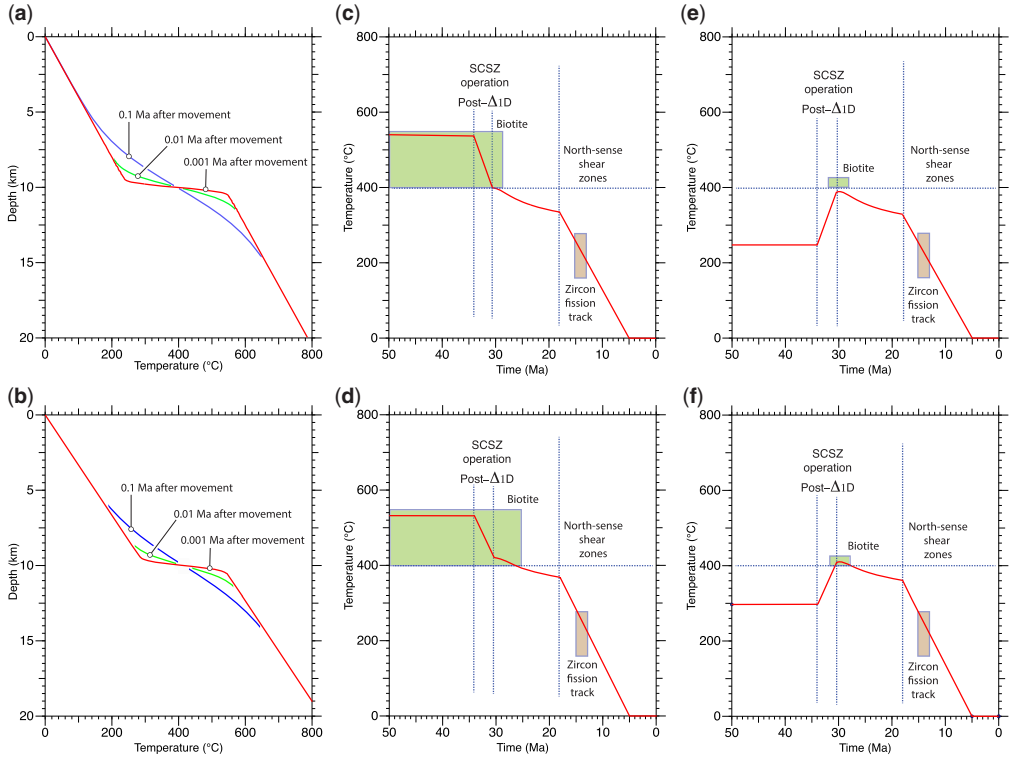

Fig. 15. Thermal evolution across an extensional detachment, based on Voorhoeve & Houseman (1988). The calculations (**a, b**) assume instantaneous displacement on a detachment fault: (a) with relative displacement of 30 km on a fault dipping at 22.5° in a 25°C/km geotherm; and (b) 16 km on a fault dipping at 30° in a 30°C geotherm. The inferred temperature history of a rock 100 m below (**c, d**) and 100 m above (**e, f**) the detachment fault. A separate overlying detachment accomplishes final exhumation from 18 to 5 Ma.

shear zone evolution. Conversely, rocks below a major detachment will be hotter than those above, but they will cool rapidly during shear zone evolution (Fig. 15c, d). Hence, using the terminology of tectonic sequence diagrams (Forster & Lister 2008), microstructures below a detachment will reflect ΔSZ sequences (Lister & Forster 2009) where Δ is an episode of mineral growth, and SZ is an overprinting shear band. In contrast rocks above a major detachment will be cooler than those below, so they will heat rapidly during shear zone evolution. Temperature remains high, even when detachment faulting has ceased, so SZΔ sequences are found, e.g. growth of small euhedral garnets that statically overprint late-formed shear bands. Microstructures forming in the upper plate during ongoing detachment may also reflect ΔSZ sequences, and form because the locus of relative movement shifts. Indicator minerals will nevertheless indicate steadily rising temperature. Late-stage shear bands are observed that begin with chlorite growth followed by growth of biotite in the shear plane (Fig. 14).

Rocks in the lower plate develop S-C mylonite fabrics, whereas rocks in the upper plate tend to stew, with mineral growth and veining driven by hot fluids moving upwards. Because temperatures rapidly average across the detachment–fault interface, mineral parageneses that reflect these fluid emanations also record the conditions at the base of the detachment. In the Plakato region, Δ_{1D} assemblages have formed in cross-cutting veins at the base of the upper plate. The Δ_{1D} episode of high-pressure metamorphic mineral growth took place under transitional blueschist–greenschist facies (Evans 1990) and was recorded as a separate event by Forster & Lister (1999*b*). The Eocene Oligocene timing of Δ_{1D} was inferred by Forster & Lister (2005), matching the timing of the start of SCSZ operation as inferred by Forster & Lister (2009). However, the earlier Δ_{1C} blueschist facies assemblages at the base of the upper plate are also overprinted by biotite-stable shear bands (Fig. 14), during south-directed shear in the SCSZ. This requires either continual operation of the SCSZ into the Miocene or a

separate pulse of activity on the SCSZ at the start of the Miocene (Fig. 4).

Figure 14 also illustrates the difficulty of reaching biotite-stable conditions (exceeding 400°C) or garnet + biotite (*c.* 450°C) at the base of the upper plate. The lower plate needs to have been at temperatures exceeding *c.* 500–550°C to allow conductive relaxation in consequence of juxtaposition to heat the base of the upper plate to 400–420°C. The observed overprint by biotite-bearing assemblages thus requires the upper plate to have been at a depth of no more than 8–10 km, at temperatures of *c.* 250–300°C by this time, which means that the upper plate must have been significantly exhumed in order to allow it to be cool in comparison with the lower plate at the time of SCSZ operation. Otherwise the development of biotite-bearing assemblages would have been more pervasive throughout the upper plate, instead of being found only within a few metres of its base. These observations further support the contention that the SCSZ operated as an extensional detachment.

Phengite v. muscovite diffusion parameters

Uunk *et al.* (2018) used muscovite parameters as determined by Harrison *et al.* (2009) to model results for their phengite geochronology on Syros. The effect of different *P–T–t* paths was modelled using activation volume to correct for the effects of pressure. Uunk *et al.* (2018) require cooling below greenschist facies temperatures before closure occurs. This result can be extrapolated to the eclogite–blueschist unit on Ios, in which case exhumation-related cooling would need to have occurred at least 8–10 myr earlier than the onset of the operation of the SCSZ. In this case, the rocks over-riding the SCSZ would have been colder than the rocks beneath, i.e. requiring the SCSZ to be an extensional shear zone.

There is a problem with this conclusion, however. If phengite is as retentive of argon as data recorded by Forster & Lister (2013) seem to imply, phengite would have grown below its nominal closure temperature range, and thermochronological inferences would not be possible. Argon geochronology would allow direct dating of the time of recrystallization and grain growth. Forster & Lister (2013) show that muscovite sub-spectra can be obtained from finely interlayered phengite-muscovite mixtures, but only if the step-heating schedule is designed so as to uniformly populate the Arrhenius plot, and to ensure similar gas release percentages in as many steps as possible in the derivative age spectrum. The muscovite sub-spectrum is not easily recognized if the Arrhenius plot is sparsely or irregularly populated.

The role of excess argon

There is evidence for extraneous ^{40}Ar accumulation in and adjacent to the Ios basement terrane (Laurent *et al.* 2017). This is ^{40}Ar in excess of the amount in the sample owing to atmospheric contamination, as determined by the ^{36}Ar/^{40}Ar ratio on the York plot, and the radiogenic ^{40}Ar* held in the lattice, produced by radioactive decay. While 'excess argon' can readily be determined in fluid inclusions, it is more difficult to separate during a UHV experiment. Excess argon can be recognized in the early cleaning steps, when isothermal duplicates are used in the step-heating schedule (Figs 7 & 10). It has not been recognized in the retentive domains of the potassium feldspar analysed in this paper. In respect to the excess ^{40}Ar released during the early stages of an individual UHV experiment, it is evident that it does not sit in the lattice, since the release of the artificially produced ^{39}Ar is not congruent with the ^{40}Ar percentage release.

Comparison with Rb–Sr thermochronology

Thomson *et al.* (2009) conducted detailed thermochronology on Ios, with differing conclusions from those reached by Baldwin & Lister (1998) or Forster & Lister (2009). The main points of contention have to do with the interpretation of the significance of the results obtained using individual geochronometers. We agree that Rb–Sr methods can be used to 'date the waning stages of mylonitic deformation' (cf Thomson *et al.* 2009) but we challenge the relevance of their conclusion that the Rb–Sr system in 'white mica is thermally stable to temperatures of c. 550° C'. The mineral has a propensity to recrystallize, dependent on the nature of the grain boundary fluid and/or the effects of plastic deformation of the mineral or the adjacent matrix. Paradoxical effects also result owing to advective fluid transport in mylonites, as noted by Müller *et al.* (1999) or Eberlei *et al.* (2015).

The Rb–Sr system is complex because the two processes involved (diffusive mass transfer through individual grains and advective mass transport through the grain boundary network) behave as a simple two-state Markov chain, e.g. http://setosa.io/ev/markov-chains/. Further, the two processes that govern the outcome take place on different scales, with differing kinetics. The effect of advection is greater when aqueous fluids are involved, because the ionic species involved are considerably more soluble.

Carbonate mylonites minimize the effect of H_2O so the effects of advection are minimized, and the age obtained using Rb–Sr geochronology is usually the same as that obtained using ^{40}Ar/^{39}Ar geochronology on phengite. This is the case for the post-Δ_{1D}

shear zone that creates and then reorients a blue-amphibole lineation in the carapace of the Varvara boudin where Thomson *et al.* (2009) report a 34.5 ± 2.5 Ma age using Rb–Sr methods, thereby obtaining the same estimate as was obtained using $^{40}Ar/^{39}Ar$ geochronology (Forster & Lister 2009). Another example in which Rb–Sr geochronology gives the same estimates as obtained using $^{40}Ar/^{39}Ar$ geochronology comes from Syros (Cliff *et al.* 2017). Lister & Forster (2016) showed that several distinct microstructural growth episodes can be recognized in these rocks: (i) phengite growth at *c.* 53 Ma associated with the Δ_{1B} eclogite facies event; (ii) decussate recrystallization leading to intergrowth of phengite at *c.* 46 Ma associated with the Δ_{1C} glaucophane + garnet facies event sequence; followed by (iii) porphyroblastic growth of white mica at *c.* 42 Ma, also associated with the Δ_{1C} glaucophane + garnet facies event sequence. Although Cliff *et al.* (2017) did not use TSDs, their microstructures are similar to what we observe, and there is a remarkable coincidence of ages obtained using Rb–Sr methods with those recorded by microstructurally focussed $^{40}Ar/^{39}Ar$ geochronology using the method of asymptotes and limits, e.g. in the Gria Spilia.

In contrast, when H_2O dominates the pore fluid, younger ages are obtained, e.g. Thomson *et al.* (2009) report *c.* 18–19 Ma ages in north-sense shear zones that overprint the dominantly south-sense SCSZ. Müller *et al.* (1999) used Rb–Sr methods on white mica and co-existing phases in mylonites deformed at temperatures as low as 350°C and obtained consistent results. In contrast $^{40}Ar/^{39}Ar$ geochronology using phengite showed much older Variscan ages, with the characteristic 'camel-hump' age spectra that result from step-heating finely intergrown phengite–muscovite mixtures (Forster & Lister 2013). The age obtained for the muscovite component is a maximum age, broadly consistent with the result for Rb–Sr geochronology reported by Müller *et al.* (1999).

We suggest these data reflect the efficacy of ionic transport in H_2O that advected through the mylonites, with transfer of material driven by changes in the pattern of grain-scale microdilatancy. In the case of mylonitic rocks with variable grain size, the effects of recrystallization of individuals grains has also to be taken into account. Heterogeneity in the inferred age distribution can reflect the presence of relict cores in individual grains, just as well as homogeneity in the inferred age distribution can reflect the absence of such relicts. Hence it is difficult to interpret the results of Rb–Sr geochronology without considering the effects of the last deformation in opening the system to advective mass transport, i.e. allowing a flux of material to move along grain boundaries and thereby re-establishing local equilibria.

Interestingly, the age obtained using Rb–Sr methods is similar to estimates of the timing of overprinting north-sense ductile shear zones on the basis of $^{40}Ar/^{39}Ar$ geochronology. The switch to north-directed extension might therefore have been abrupt, in Early Miocene time, throwing light on the debate as to the relation of the Ios core complex with its cousins on Naxos and Paros (Jolivet *et al.* 2004*a*, *b*) or with those in the west (Grasemann *et al.* 2012).

Conclusion

Modelling based on UHV diffusion experiments using potassium feldspar provided data that allowed conjoint inversion of the apparent age spectra provided by simultaneous $^{40}Ar/^{39}Ar$ geochronology. We demonstrated two periods of rapid cooling in the lower plate, and we have shown that rapid cooling took place in the lower plate during these two periods when the SCSZ was active. Hence the SCSZ was extensional, in both episodes of its operation. There is no evidence that it ever acted as a thrust.

The thermal structure during the Eocene–Oligocene transition involves hot-rocks being extracted from beneath colder rocks, attested to by the static growth of Δ_{1D} transitional blueschist–greenschist assemblages in veins emanating from the basal detachment, and in disseminated pockets, showing that the eclogite–blueschist unit had 'stewed' in fluids under those conditions of pressure and temperature. In addition, during later south-sense SCSZ operation, in Oligo-Miocene time, biotite ± garnet grew in shear bands at the base of the eclogite–blueschist unit. Metamorphic microstructures thus show the bottom of the upper plate was heated during these periods of movement, as expected if the shear zone acted as an extensional detachment, juxtaposing a hot lower plate against a cooler upper plate. The results documented in this paper thus continue to support the hypothesis that the basement schists and gneisses of central Ios were exhumed beneath the SCSZ, with relicts of the tectonic sheets of the eclogite–blueschist unit stranded above.

Acknowledgments Support from an Australian Research Council Discovery Project, DP120101875. Technical assistance provided by Davood Vasegh in the Argon Lab. The paper was improved by comments from Clare Bond, Jan Wijbrans and an anonymous reviewer.

References

Aravadinou, E., Xypolias, P., Chatzaras, V., Iliopoulos, I. & Gerogiannis, N. 2016. Ductile nappe stacking and refolding in the Cycladic Blueschist Unit: insights from Sifnos Island (south Aegean Sea). *International*

Journal of Earth Sciences, **105**, 2075–2096, https://doi.org/10.1007/s00531-015-1255-2

Augier, R., Jolivet, L., Gadenne, L., Lahfid, A. & Driussi, O. 2015. Exhumation kinematics of the Cycladic Blueschists unit and back-arc extension, insight from the Southern Cyclades (Sikinos and Folegandros Islands, Greece). *Tectonics*, **34**, 152–185, https://doi.org/10.1002/2014TC003664

Avigad, D. 1993. Tectonic juxtaposition of blueschists and greenschists in Sifnos Island (Aegean Sea) – implications for the structure of the Cycladic Blueschist belt. *Journal of Structural Geology*, **15**, 1459–1469, https://doi.org/10.1016/0191-8141(93)90006-V

Avigad, D., Garfunkel, Z., Jolivet, L. & Azañon, J.M. 1997. Back-arc extension and denudation of Mediterranean eclogites. *Tectonics*, **16**, 924–941, https://doi.org/10.1029/97TC02003

Baldwin, S.L. & Lister, G.S. 1998. Thermochronology of the South Cyclades Shear Zone, Ios, Greece: effects of ductile shear in the argon partial retention zone. *Journal of Geophysical Research: Solid Earth*, **103**, 7315–7336, https://doi.org/10.1029/97JB03106

Brun, J.-P. & Faccenna, C. 2008. Exhumation of high-pressure rocks driven by slab rollback. *Earth and Planetary Science Letters*, **272**, https://doi.org/10.1016/j.epsl.2008.02.038

Brun, J.-P., Faccenna, C. *et al.* 2016. The two-stage Aegean extension, from localized to distributed, a result of slab rollback acceleration. *Canadian Journal of Earth Sciences*, **53**, 1142–1157, https://doi.org/10.1139/cjes-2015-0203

Buick, I. 1991. Mylonite fabric development on Naxos, Greece. *Journal of Structural Geology*, **13**, 643–655, https://doi.org/10.1016/0191-8141(91)90027-G

Chatzaras, V., Xypolias, P. & Doutsos, T. 2006. Exhumation of high-pressure rocks under continuous compression: a working hypothesis for the southern Hellenides (central Crete, Greece). *Geol. Mag.*, **143**, 859–876, https://doi.org/10.1017/S0016756806002585

Cliff, R.A., Bond, C.E., Butler, R.W.H. & Dixon, J.E. 2017. Geochronological challenges posed by continuously developing tectonometamorphic systems: insights from Rb–Sr mica ages from the Cycladic Blueschist Belt, Syros (Greece). *Journal of Metamorphic Geology*, **35**, 197–211, https://doi.org/10.1111/jmg.12228

Davis, G.A., Lister, G.S. & Reynolds, S.J. 1986. Structural evolution of the Whipple and South Mountains shear zones, southwestern United States. *Geology*, **14**, 7–10, https://doi.org/10.1130/0091-7613(1986)14<7:SEOTWA>2.0.CO;2

Davis, G.H. 1983. Shear-zone model for the origin of metamorphic core complexes. *Geology*, **11**, 342–347, https://doi.org/10.1130/0091-7613(1983)11<342:SMFTOO>2.0.CO;2

Davis, G.H., Gardulski, A.F. & Lister, G.S. 1987. Shear zone origin of quartzite mylonite and mylonitic pegmatite in the Coyote Mountains metamorphic core complex, Arizona. *Journal of Structural Geology*, **9**, 289–297, https://doi.org/10.1016/0191-8141(87)90053-8

Eberlei, T., Habler, G., Wegner, W., Schuster, R., Körner, W., Thöni, M. & Abart, R. 2015. Rb/Sr isotopic and compositional retentivity of muscovite during deformation. *Lithos*, **227**, 161–178, https://doi.org/10.1016/j.lithos.2015.04.007

Edwards, M.A. & Grasemann, B. 2009. Mediterranean snapshots of accelerated slab retreat: subduction instability in stalled continental collision. *In*: Van Hinsbergen, D.J.J., Edwards, M.A. & Govers, R. (eds) *Collision and Collapse at the Africa–Arabia–Eurasia Subduction Zone*. Geological Society, London, Special Publications, **311**, 155–192, https://doi.org/10.1144/SP311.6

Evans, B.W. 1990. Phase relations of epidote–blueschists. *Lithos*, **25**, 3–23, https://doi.org/10.1016/0024-4937(90)90003-J

Forster, M.A. & Lister, G.S. 1999*a*. Detachment faults in the Aegean core complex of Ios, Cyclades, Greece. *In*: Ring, U., Brandon, M.T., Lister, G.S. & Willett, S.D. (eds) *Exhumation Processes: Normal Faulting, Ductile Flow and Erosion*. Geological Society, London, Special Publications, **154**, 305–323, https://doi.org/10.1144/GSL.SP.1999.154.01.14

Forster, M.A. & Lister, G.S. 1999*b*. Separate episodes of eclogite and blueschist facies metamorphism in the Aegean metamorphic core complex of Ios, Cyclades, Greece. *In*: Mac Niocaill, C. & Ryan, P. D. (eds) *Continental Tectonics*. Geological Society, London, Special Publications, **164**, 157–177, https://doi.org/10.1144/GSL.SP.1999.164.01.09

Forster, M.A. & Lister, G.S. 2004. The interpretation of $^{40}Ar/^{39}Ar$ apparent age spectra produced by mixing: application of the method of asymptotes and limits. *Journal of Structural Geology*, **26**, 287–305, https://doi.org/10.1016/j.jsg.2003.10.004

Forster, M.A. & Lister, G.S. 2005. Several distinct tectono-metamorphic slices in the Cycladic eclogite–blueschist belt, Greece. *Contributions to Mineralogy and Petrology*, **150**, 523–545, https://doi.org/10.1007/s00410-005-0032-9

Forster, M.A. & Lister, G.S. 2008. Tectonic sequence diagrams and the structural evolution of schists and gneisses in multiply deformed terranes. *Journal of the Geological Society*, **165**, 923–939, https://doi.org/10.1144/0016-76492007-016

Forster, M. & Lister, G. 2009. Core-complex-related extension of the Aegean lithosphere initiated at the Eocene-Oligocene transition. *Journal of Geophysical Research: Solid Earth*, **114**, https://doi.org/10.1029/2007JB005382

Forster, M.A. & Lister, G.S. 2010. Argon enters the retentive zone: reassessment of diffusion parameters for K-feldspar in the South Cyclades Shear Zone, Ios, Greece. *In*: Spalla, M.I., Marotta, A.M. & Gosso, G. (eds) *Advances in Interpretation of Geological Processes: Refinement of Multi-scale Data and Integration in Numerical Modelling*. Geological Society, London, Special Publications, **332**, 17–34, https://doi.org/10.1144/SP332.2

Forster, M.A. & Lister, G.S. 2013. $^{40}Ar/^{39}Ar$ geochronology and the diffusion of ^{39}Ar in phengite–muscovite intergrowths during step-heating experiments in vacuo. *In*: Jourdan, F., Mark, D.F. & Verati, C. (eds) *Advances in $^{40}Ar/^{39}Ar$ Dating: from Archaeology to Planetary Sciences*. Geological Society, London, Special Publications, **378**, 117–135, https://doi.org/10.1144/SP378.16

Forster, M.A., White, L.T. & Ahmad, T. 2011. Thermal history of a pebble in the Indus Molasse at the margin of a Himalayan metamorphic core complex. *Journal of the Virtual Explorer, Electronic Edition*, **38**, paper 6. *In*: Forster, M.A. & Fitz Gerald, J.D. (eds) *The Science of Microstructure – Part II*.

Forster, M., Armstrong, R., Kohn, B., Lister, G., Cottam, M. & Suggate, S. 2015. Highly retentive core domains in K-feldspar and their implications for $^{40}Ar/^{39}Ar$ thermochronology illustrated by determining the cooling curve for the Capoas Granite, Palawan, The Philippines. *Australian Journal of Earth Sciences*, **62**, 883–902, https://doi.org/10.1080/08120099.2015.1114524

Gautier, P. & Brun, J.-P. 1994. Crustal-scale geometry and kinematics of late-orogenic extension in the central Aegean (Cyclades and Evia Island). *Tectonophysics*, **238**, 399–424, https://doi.org/10.1016/0040-1951(94)90066-3

Gautier, P., Brun, J.P. & Jolivet, L. 1993. Structure and kinematics of upper Cenozoic extensional detachment on Naxos and Paros (Cyclades Islands, Greece). *Tectonics*, **12**, 1180–1194, https://doi.org/10.1029/93TC01131

Grasemann, B., Schneider, D.A., Stöckli, D.F. & Iglseder, C. 2012. Miocene bivergent crustal extension in the Aegean: evidence from the western Cyclades (Greece). *Lithosphere*, **4**, 23–39, https://doi.org/10.1130/L164.1

Groppo, C., Forster, M., Lister, G. & Compagnoni, R. 2009. Glaucophane schists and associated rocks from Sifnos (Cyclades, Greece): new constrains on the *P–T* evolution from oxidized systems. *Lithos*, **109**, 254–273, https://doi.org/10.1016/j.lithos.2008.10.005

Guo, L., Zhang, J. & Zhang, B. 2008. Structures, kinematics, thermochronology and tectonic evolution of the Ramba gneiss dome in the northern Himalaya. *Progress in Natural Science*, **18**, 851–860, https://doi.org/10.1016/j.pnsc.2008.01.016

Harrison, T.M., Célérier, J., Aikman, A.B., Hermann, J. & Heizler, M.T. 2009. Diffusion of ^{40}Ar in muscovite. *Geochimica et Cosmochimica Acta*, **73**, 1039–1051, https://doi.org/10.1016/j.gca.2008.09.038

Hobbs, B.E. 2019. The development of structural geology and the historical context of the journal of structural geology: a reflection by Bruce Hobbs. *Journal of Structural Geology*, https://doi.org/org/10.1016/j.jsg.2018.12.008

Huet, B., Labrousse, L. & Jolivet, L. 2009. Thrust or detachment? Exhumation processes in the Aegean: insight from a field study on Ios (Cyclades, Greece). *Tectonics*, **28**. TC3007, https://doi.org/10.1029/2008TC00 2397

Huet, B., Labrousse, L., Monié, P., Malvoisin, B. & Jolivet, L. 2015. Coupled phengite ^{40}Ar–^{39}Ar geochronology and thermobarometry: *P–T–t* evolution of Andros Island (Cyclades, Greece). *Geological Magazine*, **152**, 711–727, https://doi.org/10.1017/S0016756814000661

Husson, L., Brun, J.-P., Yamato, P. & Faccenna, C. 2009. Episodic slab rollback fosters exhumation of HP–UHP rocks. *Geophysical Journal International*, **179**, 1292–1300, https://doi.org/10.1111/j.1365-246X.2009.04372.x

Jolivet, L. & Brun, J.-P. 2010. Cenozoic geodynamic evolution of the Aegean. *International Journal of Earth Science*, **99**, 109–138, https://doi.org/10.1007/s00531-008-0366-4

Jolivet, L. & Faccenna, C. 2000. Mediterranean extension and the Africa–Eurasia collision. *Tectonics*, **19**, 1095–1106, https://doi.org/10.1029/2000TC900018

Jolivet, L., Maluski, H., Beyssac, O., Goffé, B., Lepvrier, C., Thi, P.T. & Vuong, N.V. 1999. Oligocene–Miocene Bu Khang extensional gneiss dome in Vietnam: geodynamic implications. *Geology*, **27**, 67–70, https://doi.org/10.1130/0091-7613(1999)027<0067:OMBKEG>2.3.CO;2

Jolivet, L., Faccenna, C., Goffé, B., Burov, E. & Agard, P. 2003. Subduction tectonics and exhumation of high-pressure metamorphic rocks in the Mediterranean orogens. *American Journal of Science*, **303**, 353–409, https://doi.org/10.2475/ajs.303.5.353

Jolivet, L., Famin, V., Mehl, C., Parra, T., Aubourg, C., Hébert, R. & Philippot, P. 2004*a*. Progressive strain localisation, boudinage and extensional metamorphic complexes, the Aegean Sea case. *In*: Whitney, D.L., Teyssier, C. & Siddoway, C.S. (eds) *Gneiss Domes in Orogeny: Boulder, Colorado*. Geological Society of America, 185–210, https://doi.org/10.1130/0-8137-2380-9.185

Jolivet, L., Famin, V., Mehl, C., Parra, T., Aubourg, C., Hébert, R. & Philippot, P. 2004*b*. Strain localization during crustal-scale boudinage to form extensional metamorphic domes in the Aegean Sea. *In*: Whitney, D.L., Teyssier, C. & Siddoway, C.S. (eds) *Gneiss Domes in Orogeny*. Geological Society of America, Boulder, CO, Special Papers, **380**, 185–210.

Jolivet, L., Lecomte, E. *et al.* 2010. The North Cycladic detachment system. *Earth and Planetary Science Letters*, **289**, 87–104, https://doi.org/10.1016/j.epsl.2009.10.032

Jolivet, L., Faccenna, C. *et al.* 2013. Aegean tectonics: strain localisation, slab tearing and trench retreat *Tectonophysics*, **597–598**, 1–33, https://doi.org/10.1016/j.tecto.2012.06.011

Kokkalas, S., Xypolias, P., Koukouvelas, I. & Doutsos, T. 2006. Postcollisional contractional and extensional deformation in the Aegean region. *In*: Dilek, Y. & Pavlides, S. (eds) *Post-Collisional Tectonics and Magmatism in the Mediterranean Region and Asia*. Geological Society of America, Boulder, CO, Special Papers, **409**, 97–123, https://doi.org/10.1130/0-8137-2409-0.97

Laurent, V., Huet, B., Labrousse, L., Jolivet, L., Monié, P. & Augier, R. 2017. Extraneous argon in high-pressure metamorphic rocks: distribution, origin and transport in the Cycladic Blueschist Unit (Greece). *Lithos*, **272–273**, 315–335, https://doi.org/10.1016/j.lithos.2016.12.013

Lee, J. & Lister, G.S. 1992. Late Miocene ductile extension and detachment faulting, Mykonos, Greece. *Geology*, **20**, 121–124, https://doi.org/10.1130/0091-7613(1992)020<0121:LMDEAD>2.3.CO;2

Lee, J., Hacker, B. & Wang, Y. 2004. Evolution of North Himalayan gneiss domes: structural and metamorphic studies in Mabja Dome, southern Tibet. *Journal of Structural Geology*, **26**, 2297–2316, https://doi.org/10.1016/j.jsg.2004.02.013

Lister, G.S. & Davis, G.A. 1989. The origin of metamorphic core complexes and detachment faults formed during Tertiary continental extension in the northern Colorado River region, USA. *Journal of Structural Geology*, **11**, 65–94, https://doi.org/10.1016/0191-8141(89)90036-9

Lister, G. & Forster, M. 2009. Tectonic mode switches and the nature of orogenesis. *Lithos*, **113**, 274–291, https://doi.org/10.1016/j.lithos.2008.10.024

Lister, G. & Forster, M. 2016. White mica $^{40}Ar/^{39}Ar$ age spectra and the timing of multiple episodes of high-P metamorphic mineral growth in the Cycladic eclogite–blueschist belt, Syros, Aegean Sea, Greece. *Journal of Metamorphic Geology*, **34**, 401–421, https://doi.org/10.1111/jmg.12178

Lister, G.S., Banga, G. & Feenstra, A. 1984. Metamorphic core complexes of Cordilleran type in the Cyclades, Aegean Sea, Greece. *Geology*, **12**, 221–225, https://doi.org/10.1130/0091-7613(1984)12<221:MCCOCT>2.0.CO;2

Lister, G., Forster, M. & Rawling, T. 2001. Episodicity during orogenesis. *In*: Miller, J.A., Holdsworth, R.E., Buick, I.S. & Hand, M. (eds) *Continental Reactivation and Reworking*. Geological Society, London, Special Publications, **184**, 89–113, https://doi.org/10.1144/GSL.SP.2001.184.01.06

Lovera, O.M., Grove, M., Harrison, T.M. & Mahon, K. 1997. Systematic analysis of K-feldspar $^{40}Ar^{39}Ar$ step heating results: I. Significance of activation energy determinations. *Geochimica et Cosmochimica Acta*, **61**, 3171–3192, https://doi.org/10.1016/S0016-7037(97)00147-6

Lovera, O.M., Grove, M. & Harrison, T.M. 2002. Systematic analysis of K-feldspar $^{40}Ar/^{39}Ar$ step heating results II: relevance of laboratory argon diffusion properties to nature. *Geochimica et Cosmochimica Acta*, **66**, 1237–1255, https://doi.org/10.1016/S0016-7037(01)00846-8

Mascle, J. & Martin, L. 1990. Shallow structure and recent evolution of the Aegean Sea: a synthesis based on continuous reflection profiles. *Marine Geology*, **94**, 271–299, https://doi.org/10.1016/0025-3227(90)90060-W

Müller, W., Dallmeyer, R.D., Neubauer, F. & Thöni, M. 1999. Deformation-induced resetting of Rb/Sr and $^{40}Ar/^{39}Ar$ mineral systems in a low-grade, polymetamorphic terrane (Eastern Alps, Austria). *Journal of the Geological Society*, **156**, 261–278, https://doi.org/10.1144/gsjgs.156.2.0261

Ramsay, J.G.M. & Huber, M.I. 1987. *The Techniques of Modern Structural Geology: Volume 2: Folds and Fractures*. Academic Press, London.

Rawling, T. & Lister, G. 1999. Oscillating modes of orogeny in the Southwest Pacific and the tectonic evolution of New Caledonia. *In*: Ring, U., Brandon, M.T., Lister, G.S. & Willett, S.D. (eds) *Exhumation Processes: Normal Faulting, Ductile Flow and Erosion*. Geological Society, London, Special Publications, **154**, 109–127, https://doi.org/10.1144/GSL.SP.1999.154.01.05

Reiners, P.W. & Brandon, M.T. 2006. Using thermochronology to understand orogenic erosion. *Annual Reviews of Earth and Planetary Science*, **34**, 419–466, https://doi.org/10.1146/annurev.earth.34.031405.125202

Reynolds, S.J. & Lister, G.S. 1990. Folding of mylonitic zones in Cordilleran metamorphic core complexes: evidence from near the mylonitic front. *Geology*, **18**, 216–219, https://doi.org/10.1130/0091-7613(1990)018<0216:FOMZIC>2.3.CO;2

Ring, U., Glodny, J., Will, T. & Thomson, S. 2010. The Hellenic subduction system: high-pressure metamorphism, exhumation, normal faulting and large-scale extension. *Annual Review of Earth and Planetary Sciences*, **38**, 45–76, https://doi.org/10.1146/annurev.earth.050708.170910

Ring, U., Glodny, J., Will, T.M. & Thomson, S. 2011. Normal faulting on Sifnos and the South Cycladic Detachment System, Aegean Sea, Greece. *Journal of the Geological Society*, **168**, 751–768, https://doi.org/10.1144/0016-76492010-064

Roche, V., Laurent, V., Cardello, G.L., Jolivet, L. & Scaillet, S. 2016. Anatomy of the Cycladic Blueschist Unit on Sifnos Island (Cyclades, Greece). *Journal of Geodynamics*, **97**, 62–87, https://doi.org/10.1016/j.jog.2016.03.008

Rosenbaum, G. & Ring, U. 2007. Structure and metamorphism of Amorgos: a field excursion. *Journal of the Virtual Explorer*, **27**, paper 7. https://doi.org/10.3809/jvirtex.2007.00181

Schliestedt, M. & Matthews, A. 1987. Transformation of blueschist to greenschist facies rocks as a consequence of fluid infiltration, Sifnos (Cyclades), Greece. *Contributions to Mineralogy and Petrology*, **97**, 237–250, https://doi.org/10.1007/BF00371243

Schmädicke, E. & Will, T.M. 2003. Pressure–temperature evolution of blueschist facies rocks from Sifnos, Greece, and implications for the exhumation of high-pressure rocks in the Central Aegean. *Journal of Metamorphic Geology*, **21**, 799–811, https://doi.org/10.1046/j.1525-1314.2003.00482.x

Schneider, D., Senkowski, C., Vogel, H., Grasemann, B. & Iglseder, C. 2011. Eocene tectonometamorphism on Serifos (western Cyclades) deduced from zircon depth-profiling geochronology and mica thermochronology. *Lithos*, **125**, 151–172, https://doi.org/10.1016/j.lithos.2011.02.005

Schneider, D.A., Grasemann, B., Lion, A., Soukis, K. & Draganits, E. 2018. Geodynamic significance of the Santorini Detachment System (Cyclades, Greece). *Terra Nova*, **30**, 414–422, https://doi.org/10.1111/ter.12357

Thomson, S.N., Ring, U., Brichau, S., Glodny, J. & Will, T.M. 2009. Timing and nature of formation of the Ios metamorphic core complex, southern Cyclades, Greece. *In*: Ring, U. & Wernicke, B. (eds) *Extending a Continent: Architecture, Rheology and Heat Budget*. Geological Society, London, Special Publications, **321**, 139–167, https://doi.org/10.1144/SP321.7

Urai, J., Schuiling, R. & Jansen, J. 1990. Alpine deformation on Naxos (Greece). *In*: Knipe, R.J. & Rutter, E.H. (eds) *Deformation Mechanisms, Rheology and Tectonics*. Geological Society, London, Special Publications, **54**, 509–522, https://doi.org/10.1144/GSL.SP.1990.054.01.47

Uunk, B., Brouwer, F., Voorde, M. & Wijbrans, J. 2018. Understanding phengite argon closure using single grain fusion age distributions in the Cycladic Blueschist Unit on Syros, Greece. *Earth and Planetary Science*

Letters, **484**, 192–203, https://doi.org/10.1016/j.epsl.2017.12.031

Vandenberg, L.C. & Lister, G.S. 1996. Structural analysis of basement tectonites from the Aegean metamorphic core complex of Ios, Cyclades, Greece. *Journal of Structural Geology*, **18**, 1437–1454, https://doi.org/10.1016/S0191-8141(96)00068-5

Verdel, C., Wernicke, B.P., Ramezani, J., Hassanzadeh, J., Renne, P.R. & Spell, T.L. 2007. Geology and thermochronology of Tertiary Cordilleran-style metamorphic core complexes in the Saghand region of central Iran. *Geological Society of America Bulletin*, **119**, 961–977, https://doi.org/10.1130/B26102.1

Voorhoeve, H. & Houseman, G. 1988. The thermal evolution of lithosphere extending on a low-angle detachment zone. *Basin Research*, **1**, 1–9, https://doi.org/10.1111/j.1365-2117.1988.tb00001.x

Walcott, C.R. & White, S.H. 1998. Constraints on the kinematics of post-orogenic extension imposed by stretching lineations in the Aegean region. *Tectonophysics*, **298**, 155–175, https://doi.org/10.1016/S0040-1951(98)00182-6

Xypolias, P., Iliopoulos, I., Chatzaras, V. & Kokkalas, S. 2012. Subduction- and exhumation-related structures in the Cycladic Blueschists: insights from south Evia Island (Aegean region, Greece). *Tectonics*, **31**, TC2001, https://doi.org/10.1029/2011TC002946